Nuclear Science and Techniques (2025) 36:56
https://doi.org/10.1007/s41365-025-01665-9

Reduced-width amplitude in nuclear cluster physics

De-Ye Tao[1] · Bo Zhou[1,2]

Received: 22 September 2024 / Revised: 23 October 2024 / Accepted: 25 October 2024 / Published online: 22 February 2025

Abstract
As a cluster overlap amplitude, the reduced-width amplitude is an important physical quantity for analyzing clustering in the nucleus depending on specified channels and has been calculated and widely applied in nuclear cluster physics. In this review, we briefly revisit the theoretical framework for calculating the reduced-width amplitude, as well as the outlines of cluster models to obtain microscopic or semi-microscopic cluster wave functions. We also introduce the recent progress related to cluster overlap amplitudes, including the implementation of cross-section estimation and extension to three-body clustering analysis. Comprehensive examples are provided to demonstrate the application of the reduced-width amplitude in analyzing clustering structures.

Keywords Nuclear clustering · Microscopic cluster model · Reduced-width amplitude

1 Introduction

Clustering is one of the most important aspects of understanding nuclear structures [1, 2]. Clustering fundamentally affects the structure and reaction features of stable and unstable exotic nuclei.

Since the 1960s, various cluster models [3, 4] have been proposed and applied to the study of exotic nuclear structures that cannot be understood from the perspective of a pure shell model. Currently, clustering effects play an increasingly important role not only in nuclear structures but also in many other fields of nuclear physics, such as heavy-ion collisions [5–7], astrophysical nucleosynthesis [8, 9], and nuclear matter [10, 11].

According to cluster models, nucleons are assigned to different groups to construct clusters, and the relative motion wave function between the clusters is solved using the equation of motion. Microscopic cluster models, including the resonating group method (RGM) [12, 13] and generator coordinate method (GCM) [13–15], ensure the antisymmetrization between all the nucleons. By contrast, the orthogonality condition model (OCM) [16–18], as a semi-microscopic cluster model, simulates the effect of antisymmetrization by requiring the intercluster wave function to be orthogonal to the forbidden states. In recent years, a novel type of wave function known as the Tohsaki–Horiuchi–Schuck–Röpke (THSR) wave function proposed by Tohsaki, Horiuchi, Schuck, and Röpke [19] has been utilized for studying the well-known Hoyle state [20] and the analogous 4α gas-like state of ^{16}O. A generalized THSR wave function [21] was proposed a decade later to describe the clustering structure in nuclei [22, 23].

In nuclear physics, various physical quantities, including the root-mean-square (RMS) radius, monopole transition strength $M(E0)$, and cluster decay width, reflect the degree of clustering in the nucleus. A straightforward indicator of clustering is the reduced-width amplitude (RWA), or overlap amplitude [13, 24]. The RWA is defined as the overlap between the wave function of the nucleus and the cluster-coupling wave function in a specified channel, depending on the distance between the clusters. Accordingly, the RWA not only indicates the probability of cluster formation but also the relative motion between clusters. The radial nodal excitation of the intercluster motion can be inferred from the

This work was supported by the National Key R&D Program of China (No. 2023YFA1606701) and the National Natural Science Foundation of China (Nos. 12175042 and 12147101).

✉ Bo Zhou
zhou_bo@fudan.edu.cn

[1] Key Laboratory of Nuclear Physics and Ion-beam Application (MOE), Institute of Modern Physics, Fudan University, Shanghai 200433, China

[2] Shanghai Research Center for Theoretical Nuclear Physics, NSFC and Fudan University, Shanghai 200438, China

relationship $N = 2n + l$, where N is the principal quantum number of relative motion, n is the radial quantum number equal to the number of nodes exhibited by the RWA, and l is the quantum number of the orbital angular momentum [25]. Notably, as a quantity defined in the cluster model analysis, RWA has essentially the same physical meaning as the cluster form factor in the no-core shell model (NCSM) [26] and the overlap function in reaction theories [27].

Sharing the same definition as that of the overlap function, the RWA can also serve as an important input parameter for evaluating reaction cross sections, thus providing more accurate microscopic structural information for nuclear reaction studies [28–32]. In traditional reaction theories, such as the distorted wave Born approximation (DWBA) method [33, 34], the structural information of the participating nuclei is approximated using a simple optical-potential model, and the relative motion wave function must be normalized by an adjustable spectroscopic factor, which is fitted according to the experimental data to include the effects of antisymmetrization and core excitation [28]. Therefore, using the microscopically obtained RWA as input in reaction theories greatly enhances the precision and self-consistency of the cross-section calculations, as it incorporates more detailed information about the participating nuclei and interactions.

This article aims to provide a concise overview of the calculations and applications of the RWA. In the following section, we introduce various cluster model wave functions and the theoretical models used to obtain them. In Sect. 3, we define and discuss the calculation methods of RWA based on the cluster model wave functions. We also examine the features and extensions of the three-body analysis. Applications of RWA in clustering structure analysis are presented in Sect. 4. Finally, in Sect. 5 we provide a summary and outlook.

2 Nuclear cluster wave functions

In light nuclei, cluster configurations evolve with increasing excitation energy. The ground state generally has a compact structure, but in excited states, especially near breakup thresholds of cluster emission, various interesting clustering structures emerge, as illustrated by the famous Ikeda diagram [35].

Microscopic cluster models [1] aim to describe and understand the correlations between clusters or nucleons in states with significant clustering effects. Microscopic studies on nuclear clustering began with Wheeler's proposal of the RGM in 1937 [12]. Various cluster models have since been introduced to theoretically analyze the structure and scattering characters of light nuclei. To properly describe the nuclear system, one must consider the antisymmetrization effect in the wave function due to the indistinguishability of nucleons. The Hamiltonian of the nuclear system can be expressed as

$$\mathcal{H} = -\frac{\hbar^2}{2m}\sum_i \nabla_i^2 - T_{\text{c.m.}} + V, \tag{1}$$

where $T_{\text{c.m.}}$ denotes the kinetic energy of the center of mass (COM) motion of the nucleus and V is the interaction between nucleons, which typically includes the two-body nuclear force, Coulomb interaction, and the spin–orbit interaction. Note that the choice of nuclear force is crucial for a proper description of the nuclear system. In microscopic cluster models, effective nucleon–nucleon interactions such as Volkov No. 2 [36] and the Minnesota potential [37] are frequently adopted, in which the interaction parameters are determined by fitting fundamental features of the studied system, such as the binding energy or the phase shift of the α cluster. However, semi-microscopic cluster models disregard the internal structure of clusters. Accordingly, these theories typically treat the two-body nuclear force as a phenomenological cluster–cluster potential or infer it from nucleon–nucleon potentials through a folding procedure.

2.1 Resonating group method

The RGM was formulated as early as 1937 to study scattering between light nuclei microscopically. In this method, the nucleons are separated into several groups, as the precursor of the concept of "cluster," whereas the exchange effect between identical nucleons from different groups is taken as if the nucleon is resonating between each group. Since the 1960s, intensive research has been conducted using RGM to analyze the clustering structures of nuclei. Considering a two-cluster system $A = C_1 + C_2$, the RGM wave function is defined as [18]

$$\Psi^{\text{RGM}} = \mathcal{A}\{\phi_{C_1}\phi_{C_2}\chi(\boldsymbol{\rho})\}, \tag{2}$$

where ϕ_{C_1} and ϕ_{C_2} denote the internal wave functions of clusters C_1 and C_2 and $\chi(\boldsymbol{\rho})$ is the intercluster relative wave function, depending on the relative coordinates between the COM of the two clusters $\boldsymbol{\rho}$. The antisymmetrization operator $\mathcal{A}$ is applied to the dynamic coordinates of the nucleons between clusters C_1 and C_2. The relative wave function $\chi(\boldsymbol{\rho})$ is obtained as the solution to the equation of motion as follows:

$$\int \left[H(\boldsymbol{\rho},\boldsymbol{\rho}') - EN(\boldsymbol{\rho},\boldsymbol{\rho}')\right]\chi(\boldsymbol{\rho}')d\boldsymbol{\rho}' = 0, \tag{3}$$

where $H(\boldsymbol{\rho},\boldsymbol{\rho}')$ and $N(\boldsymbol{\rho},\boldsymbol{\rho}')$ represent the RGM kernels of Hamiltonian and normalization operators, respectively.

2.2 Generator coordinate method and Brink wave function

The actual calculation using the RGM is tedious and requires solving both an integro-differential equation and an analysis of the Hamiltonian and norm kernels. In addition, extension to three or more cluster systems within the RGM framework is much more cumbersome. The proposal of the generator coordinate method (GCM), which is essentially equivalent to the RGM [18, 38], makes performing the calculation and extending the framework to multi-cluster systems much easier. The GCM wave function of the nucleus can be expressed as [18]

$$\Psi^{\mathrm{GCM}} = \int d\alpha f(\alpha)\Phi(\alpha), \tag{4}$$

where $d\alpha = d\alpha_1 d\alpha_2 \cdots$, $\Phi(\alpha)$ is the generating wave function specified by the generator coordinates $\alpha_1, \alpha_2, \cdots$, which serve as variation parameters rather than physical coordinates. The weight function $f(\alpha)$ is determined by solving the Hill–Wheeler equation

$$\int \left[H(\alpha,\alpha') - EN(\alpha,\alpha')\right] f(\alpha')d\alpha' = 0, \tag{5}$$

where the Hamiltonian and norm kernels are defined as

$$\begin{aligned} H(\alpha,\alpha') &= \left\langle \Phi(\alpha)|\mathcal{H}|\Phi(\alpha')\right\rangle \\ N(\alpha,\alpha') &= \left\langle \Phi(\alpha)\middle|\Phi(\alpha')\right\rangle. \end{aligned} \tag{6}$$

The GCM is extensively used in the analyses of clustering structures in nuclei, combined with the Brink wave function. The Brink wave function serves as the basis wave function that is superposed to obtain the wave function of the total system. The Brink wave function is defined as a fully antisymmetrized many-body wave function consisting of several cluster wave functions characterized by various generator coordinates. For a nucleus including A nucleons with a clustering configuration of $C_1 + C_2 + \cdots + C_N$, the Brink wave function is given by [39]

$$\Phi^{\mathrm{B}}(\boldsymbol{R}_1, \cdots, \boldsymbol{R}_N) = \mathcal{A}\left\{\Phi_{C_1}(\boldsymbol{R}_1)\cdots\Phi_{C_N}(\boldsymbol{R}_N)\right\}, \tag{7}$$

where C_j $(j = 1, \cdots, N)$ denotes the jth cluster and its mass number. The wave function of cluster C_j is defined as

$$\Phi_{C_j}(\boldsymbol{R}_j) = \mathcal{A}\{\phi_1(\boldsymbol{R}_j)\cdots\phi_{C_j}(\boldsymbol{R}_j)\}, \tag{8}$$

and $\boldsymbol{R}_j$ denotes the generator coordinates. The single-particle wave function is expressed in the Gaussian form as

$$\phi_k(\boldsymbol{R}_j) = \frac{1}{(\pi b^2)^{3/4}} \exp\left[-\frac{1}{2b^2}(\boldsymbol{r}_k - \boldsymbol{R}_j)^2\right]\chi_k\tau_k \tag{9}$$

where the spins and isospins are fixed as $|\uparrow\rangle$ or $|\downarrow\rangle$. b denotes the harmonic oscillator parameter of single nucleons.

To describe a realistic nuclear system, the GCM–Brink wave function is defined as the superposition of the angular momentum and parity-projected Brink wave functions:

$$\Psi^{J\pi}_M = \sum_{i,K} c_{i,K}\hat{P}^{J\pi}_{MK}\Phi^{\mathrm{B}}(\{\boldsymbol{R}\}_i), \tag{10}$$

with the projectors defined as

$$\begin{aligned} \hat{P}^{J}_{MK} &= \frac{2J+1}{8\pi^2}\int d\Omega D^{J*}_{MK}(\Omega)\hat{R}(\Omega) \\ \hat{P}^{\pi} &= \frac{1+\pi\hat{P}_r}{2}, \quad \pi = \pm, \end{aligned} \tag{11}$$

and the index i specifies each cluster configuration indicated by a set of generator coordinates $\{\boldsymbol{R}\} = \{\boldsymbol{R}_1, \cdots, \boldsymbol{R}_N\}$. The coefficients $\{c_{i,K}\}$ are then determined by solving the Hill–Wheeler equation.

In the Brink cluster model, the existence of clusters is assumed *a priori*. By contrast, more flexible theoretical methods for studying nuclear clustering, such as antisymmetrized molecular dynamics (AMD) [40–42] and fermionic molecular dynamics (FMD) [43–45], treat all nucleons independently without assuming any clustering structure. The Brink wave function can be considered as a special case of AMD or FMD wave functions, with a fixed harmonic oscillator parameter b and frozen degrees of freedom for the nucleons in clusters.

2.3 Orthogonality condition model

In RGM and GCM, the forbidden states, resulting from the Pauli exclusion principle between fermions, are eliminated when solving the equations of motion due to antisymmetrization in the nuclear systems. As a semi-microscopic method, the orthogonality condition model (OCM) [16–18] reduces computation cost by artificially removing the forbidden states before solving the equation of motion. Considering the semi-microscopic approximation of the RGM, the equation of motion can be expressed as

$$(\mathcal{H} - E\mathcal{N})\chi = 0, \tag{12}$$

where $\mathcal{H}$ and $\mathcal{N}$ are the Hamiltonian and normalization operators, respectively. The RGM equation can be rewritten as

$$\Lambda(\mathcal{N}^{-1/2}\mathcal{H}\mathcal{N}^{-1/2} - E)\Lambda(\mathcal{N}^{1/2}\chi) = 0, \tag{13}$$

where $\Lambda \equiv 1 - \sum_F |\chi_F\rangle\langle\chi_F|$ and χ_F denote forbidden states. In OCM, we assume that the nonlocality effect of the RGM can be approximated using the orthogonality operator Λ with respect to the Pauli-forbidden space. Accordingly, before the orthogonality operation, $\mathcal{N}^{-1/2}\mathcal{H}\mathcal{N}^{-1/2}$ is first approximated by the Hamiltonian without the exchange part (e.g., with an effective localized potential V^{eff}).

$$\mathcal{N}^{-1/2}\mathcal{H}\mathcal{N}^{-1/2} \approx -\frac{\hbar^2}{2\mu}\nabla_r^2 + V^{\text{eff}}(\boldsymbol{r}). \tag{14}$$

In this case, we obtain the OCM equation

$$\Lambda\left[-\frac{\hbar^2}{2\mu}\nabla_r^2 + V^{\text{eff}}(\boldsymbol{r}) - E\right]\Lambda\left(\mathcal{N}^{1/2}\chi\right) = 0, \tag{15}$$

which is much easier to solve, even for heavier nuclei.

2.4 Tohsaki–Horiuchi–Schuck–Röpke wave function

In 2001, the THSR wave function [19] was originally proposed to describe the α-condensation of the Hoyle state, defined as

$$\begin{aligned}\Psi_{3\alpha}^{\text{THSR}}(B) &= N(B)\mathcal{A}\left\{\exp\left[-\frac{2}{B^2}\sum_{k=1}^{3}(\boldsymbol{X}_k - \boldsymbol{X}_{\text{cm}})^2\right]\prod_{i=1}^{3}\phi(\alpha_i)\right\}\end{aligned} \tag{16}$$

where $B = (b^2 + 2R_0^2)^{1/2}$ and $\boldsymbol{X}_i$ denotes the coordinates of the COM of the ith α cluster, whose internal wave function is $\phi(\alpha_i)$. It can be seen that in the THSR wave function, the three α clusters occupy the same lowest $0S$ harmonic oscillator orbit characterized by a width parameter B. When the B parameter is as large as the size of the whole nucleus, the α clusters can be considered to be moving freely in the nucleus, occupying the lowest $0S$ orbit. This behavior of α clusters is associated with the concept of Bose–Einstein condensation (BEC) of bosons. However, when B has the same value as the width parameter of the free α particle $B = b$, the THSR wave function is reduced to the Brink wave function.

An important feature of the clustering revealed by the THSR wave function is the BEC nature of the Hoyle state. It was found that by varying the total energy, the Hoyle state could be obtained using the THSR wave function with a rather large B value, which means that the Hoyle state can be well interpreted as a 3-α condensate state, where the α clusters all move in the $0S$ orbit within a relatively large volume, consistent with the large radius of the Hoyle state [19]. More interestingly, a subsequent study showed that the THSR wave function of the Hoyle state is nearly equivalent to the 3α cluster model wave functions obtained from the RGM or GCM [46]:

$$\left|\left\langle \Psi_{3\alpha}^{\text{THSR}} \middle| \Psi_{3\alpha}^{\text{RGM/GCM}} \right\rangle\right|^2 \approx 100\%. \tag{17}$$

Starting from the nonlocalized character of cluster motion, Ref. [22, 47, 48] proposed a container picture in which the size parameters $\{B_i\}$ of the cluster relative motion wave functions are considered as true dynamical quantities for describing the correlations between clusters, and the cluster correlations are also considered. In addition, by addressing the separation of the center of mass problem and considering different cluster correlations, Ref. [49] proposed a new trial wave function:

$$\begin{aligned}\Psi^{\text{new}} =& \hat{L}_{N-1}(\boldsymbol{\beta})\hat{G}_N(\beta_0)\hat{D}(\boldsymbol{Z})\Phi_0(\boldsymbol{r}) \\ =& \int d^3\tilde{T}_1 \cdots d^3\tilde{T}_{N-1} \exp\left[-\sum_{i=1}^{N-1}\frac{\tilde{T}_i^2}{\beta_i^2}\right] \\ & \int d^3R_1 \cdots d^3R_N \exp\left[-\sum_{i=1}^{N}\frac{C_i(\boldsymbol{R}_i - \boldsymbol{Z}_i - \boldsymbol{T}_i)^2}{\beta_0^2 - 2b_i^2}\right] \\ & \Phi_0(\boldsymbol{r} - \boldsymbol{R}) \\ =& n_0 \exp\left[-\frac{A}{\beta_0^2}X_{\text{cm}}^2\right] \\ & \mathcal{A}\left\{\prod_{i=1}^{N-1}\exp\left[-\frac{(\boldsymbol{\xi}_i - \boldsymbol{S}_i)^2}{2B_i^2}\right]\prod_{i=1}^{N}\phi_i^{\text{int}}(b_i)\right\},\end{aligned} \tag{18}$$

where $\hat{D}(\boldsymbol{Z})$ shifts the nucleons to the positions of the corresponding clusters, $\hat{G}_N(\beta_0)$ performs an integral transformation to separate the COM from the wave function, and $\hat{L}_{N-1}(\boldsymbol{\beta})$ describes the cluster correlations in the form of the container picture. For further details, please refer to Ref. [49]. The physical meaning of the quantities in Eq. (18) is clear. $\boldsymbol{X}_{\text{cm}}$ is the COM coordinate of the entire nucleus. $\boldsymbol{\xi}_i$ and $\boldsymbol{S}_i$ are the Jacobi coordinates of the cluster COM coordinate $\boldsymbol{X}_i$ and generator coordinate $\boldsymbol{Z}_i$, respectively. The internal wave function of the ith cluster $\phi_i^{\text{int}}(b_i)$ depends on the width variable b_i and includes the spin and isospin parts. By applying the integral, we can determine the width of the Gaussian relative wave function as follows:

$$B_k^2 = \frac{1}{2}\left[\sum_{i=1}^{k+1}C_i \Big/ \left(C_{k+1}\sum_{i=1}^{k}C_i\right)\right]\beta_0^2 + \frac{1}{2}\beta_k^2. \tag{19}$$

In the future, by utilizing this wave function, we can achieve a more realistic description of various cluster states in light nuclei.

3 Reduced-width amplitudes

Provided the microscopic wave functions are based on the aforementioned cluster models, namely $\Psi_M^{J\pi}$, the RWA of a system with a clustering structure of $A = C_1 + C_2$ is defined as follows:

$$y_{\rm c}^{J\pi}(a) = \sqrt{\frac{A!}{(1+\delta_{C_1C_2})C_1!C_2!}} \times \left\langle \frac{\delta(r-a)}{r^2}\left[Y_l(\hat{\boldsymbol{r}}) \otimes \left[\Phi_{C_1}^{j_1\pi_1} \otimes \Phi_{C_2}^{j_2\pi_2}\right]_{j_{12}}\right]_{JM}\middle|\Psi_M^{J\pi}\right\rangle, \tag{20}$$

where a is the distance between the clusters, and $c = \{j_1\pi_1 j_2\pi_2 j_{12} l\}$ denotes the coupling channel $[[C_1(j_1) \otimes C_2(j_2)]_{j_{12}} \otimes l]_J$, meaning that the clusters C_1 and C_2, with the angular momenta of j_1 and j_2, respectively, are coupled to the angular momentum of j_{12} and then coupled with the orbital angular momentum l to the total angular momentum of the nucleus J. For each channel, the nucleus and cluster parities satisfy $\pi = (-)^l\pi_1\pi_2$. $\Phi_{C_1}^{j_1\pi_1}$ and $\Phi_{C_2}^{j_2\pi_2}$ are reference wave functions of the clusters C_1 and C_2, respectively. The $(1+\delta_{C_1C_2})$ factor originates from the exchange symmetry of identical clusters $C_1 = C_2$ and is omitted in the following discussion. For clarity, we illustrate the above definitions of RWA and the coupling channel in Fig. 1.

The significance of RWA is twofold. First, the RWA provides important information about the clustering configurations and angular momentum coupling channels. The amplitudes are directly related to the probability of forming a clustering structure at different separation distances. Consequently, the optimized distance between the two-body clustering and forbidden states can be inferred from the amplitudes. To further evaluate the components of the clustering configurations in the state of a nucleus, we can calculate the spectroscopic factors (SFs) by integrating the squared norm of RWA:

$$S_{\rm c}^2 = \int_0^\infty \left|a y_{\rm c}^{J\pi}(a)\right|^2 {\rm d}a. \tag{21}$$

For narrow resonance states, according to the R-matrix theory [50], RWA and SF are important parameters for determining the decay parameters. The decay width is calculated by

$$\Gamma_{\rm c} = 2P_l(a)\gamma_{\rm c}^2(a), \tag{22}$$

with

$$P_l(a) = \frac{ka}{F_l^2(ka) + G_l^2(ka)}, \tag{23}$$

where k is the momentum of the intercluster motion in the asymptotic region and $F_l(r)$ and $G_l(r)$ are the regular and irregular Coulomb functions, respectively. $\gamma_{\rm c}^2(a)$ is the reduced width, which can be approximated using the value of RWA

$$\gamma_{\rm c}^2(a) = \frac{\hbar^2}{2\mu a}\left[a y_{\rm c}^{J\pi}(a)\right]^2, \tag{24}$$

where μ denotes the reduced masses of the two clusters. As a good measure of the cluster formation probability at the nuclear surface, the dimensionless reduced width is defined as the ratio of the reduced width to its Wigner limit $\gamma_W(a) = 3\hbar^2/2\mu a$

$$\theta_{\rm c}^2(a) \equiv \frac{\gamma_{\rm c}^2(a)}{\gamma_W^2(a)} = \frac{a}{3}\left[a y_c^{J\pi}(a)\right]^2. \tag{25}$$

Another important aspect of the RWA is its application to reaction theories, serving as the input parameter for calculating cross sections. The reduced-width amplitude essentially has a physical meaning equivalent to the overlap function, which is typically employed in reaction theories to evaluate the cross sections and is defined as [27]

$$I_{J_BJ_C}^{J_A}(\boldsymbol{r}) = \sqrt{\frac{A!}{B!C!}}\left\langle \Psi_B^{J_B}\Psi_C^{J_C}\middle|\Psi_A^{J\pi}\right\rangle = \sum_{j_{12}m_{12}lm} I_{\rm c}^{J\pi}(r)Y_{lm}(\hat{\boldsymbol{r}}). \tag{26}$$

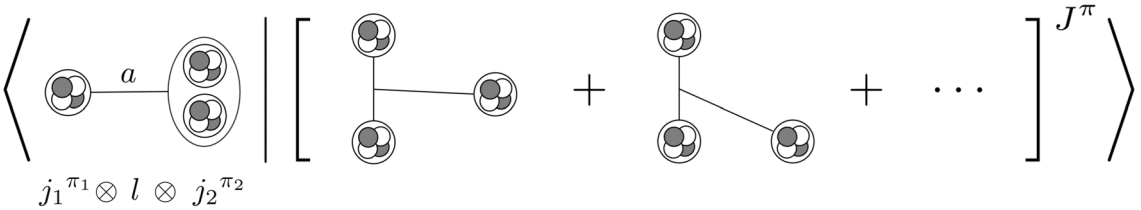

Fig. 1 (Color online) RWA, with the $\alpha + {}^8$Be structure in ^{12}C used as an example. The left side shows the channel wave function where the two clusters, with the angular momenta and parities of $j_1{}^{\pi_1}$ and $j_2{}^{\pi_2}$, respectively, are coupled together with the orbital angular momentum l. The right side shows the GCM wave function, which superposes many clustering configurations and is projected on the angular momentum and parity J^π

It is used for a reaction process in which $A = B + C$. The RWA, or overlap function, which connects the states in the entrance and exit channels, is an important constituent of the scattering or transition matrix.

For example, in the (d, p) transfer reaction, the scattering matrix from the initial state i to the final state f is [28, 51]

$$\begin{aligned} U_{i,f}^{J\pi} &= -\frac{i}{\hbar}\left\langle \Psi_f^{J\pi}\middle| V_{\rm pn} + \Delta V\middle|\Psi_i^{J\pi}\right\rangle \\ &= -\frac{i}{\hbar}\sum_{\gamma}\int u_{\gamma}^{J\pi}(R)K_{\gamma}^{J\pi}(R,R')u_f^{J\pi}(R')RR'\mathrm{d}R\mathrm{d}R', \end{aligned} \tag{27}$$

where $\Psi_i^{J\pi}$ and $\Psi_f^{J\pi}$ are the wave functions of the initial and final states, respectively, and ΔV is the remnant potential. Function $u_{\gamma}^{J\pi}(R)$ is the radial function between the target nucleus and the deuteron in the reaction channel γ, and $u_f^{J\pi}$ is the radial function between the residual nucleus and the proton. The transfer kernel is evaluated using the RWA $y_{\rm c}(r')$:

$$\begin{aligned} K_{\gamma}^{J\pi}(R,R') =& \mathcal{J}\sum_{c}\left\langle \left[\phi_k^l(\boldsymbol{r})\otimes Y_{L_i}(\Omega_R)\right]^J\middle| V_{\rm pn}\right. \\ &\left. + \Delta V\middle|\left[y_c(r')\otimes Y_{L_f}(\Omega_{R'})\right]^J\right\rangle, \end{aligned} \tag{28}$$

where $\mathcal{J}$ is the Jacobian, and ϕ_k^{lm} is the continuum discretized coupled channel (CDCC) wave function of the deuteron.

On the other hand, for (p, pα) knockout reactions, the triple-differential cross section can be evaluated using the distorted wave impulsive approximation (DWIA) [30, 52]

$$\frac{d^3\sigma}{dE_1^{\rm L}d\Omega_1^{\rm L}d\Omega_2^{\rm L}} = F_{\rm kin}C_0\frac{d\sigma_{\rm p\alpha}}{d\Omega_{\rm p\alpha}}(\theta_{\rm p\alpha},T_{\rm p\alpha})\left|\bar{T}_{\boldsymbol{K}_i}\right|^2, \tag{29}$$

where the kinematical factor $F_{\rm kin}$ is defined as

$$F_{\rm kin} = J_{\rm L}\frac{K_1K_{\alpha}E_1E_{\alpha}}{(\hbar c)^4}\left[1+\frac{E_{\alpha}}{E_{\rm B}}+\frac{E_{\alpha}}{E_{\rm B}}\frac{\boldsymbol{K}_1\cdot\boldsymbol{K}_{\alpha}}{K_{\alpha}^2}\right], \tag{30}$$

where $J_{\rm L}$ denotes the Jacobian form for the COM frame to the L frame and

$$C_0 = \frac{E_0}{(\hbar c)^2K_0}\frac{\hbar^4}{(2\pi)^3\mu_{\rm p\alpha}^2} \tag{31}$$

is a constant. $\boldsymbol{K}_i$, Ω_i, and E_i denote the wave number, its solid angle, and the total energy of particle i ($i = 0$ for incident protons, $i = 1$ for emitted protons, and $i = \alpha$ for the emitted α cluster), respectively. The reduced transition matrix is related to α-RWA by

$$\bar{T}_{\boldsymbol{K}_i} = \int d\boldsymbol{r}F_{\boldsymbol{K}_i}(\boldsymbol{r})y(r)Y_{00}(\hat{\boldsymbol{r}}), \tag{32}$$

where

$$F_{\boldsymbol{K}_i}(\boldsymbol{r}) = \chi_{1,\boldsymbol{K}_1}^{*(-)}(\boldsymbol{r})\chi_{\alpha,\boldsymbol{K}_{\alpha}}^{*(-)}(\boldsymbol{r})\chi_{0,\boldsymbol{K}_0}^{(+)}(\boldsymbol{r})e^{-i\boldsymbol{K}_0\cdot\boldsymbol{r}A_{\alpha}/A}. \tag{33}$$

$\chi_{i,\boldsymbol{K}_i}$ is the distorted wave between particles i and A for $i = 0$ and between i and B. The superscripts (+) and (−) indicate the outgoing and incoming boundary conditions of the scattered waves, respectively.

3.1 Calculation methods of RWA

Calculation methods for the RWA were established many years ago [13]. In RGM, the calculation for the RWA is straightforward, where the RGM-type wave function is written as

$$\begin{aligned} \Psi^{\rm RGM} =& \sqrt{\frac{C_1!C_2!}{A!}} \\ &\times\mathcal{A}\left\{\chi_l(r)\left[Y_l(\hat{r})\otimes\left[\Phi_{C_1}^{j_1\pi_1}\otimes\Phi_{C_2}^{j_2\pi_2}\right]_{j_{12}}\right]_{JM}\right\}. \end{aligned} \tag{34}$$

The relative motion wave function $\chi_l(r)$ can be expanded using the radial harmonic oscillator functions $R_{nl}(r,\nu')$

$$\chi_l(r) = \sum_n e_nR_{nl}(r,\nu'), \tag{35}$$

in which

$$e_n = \int R_{nl}(r,\nu')\chi_l(r)r^2dr. \tag{36}$$

and $\nu' = (C_1C_2/A)\nu$, where $\nu = 1/2b^2$ denotes the width. The RWA can then be calculated by

$$y_{\rm c}^{J\pi}(r) = \sum_n \mu_{nl}e_nR_{nl}(r,\nu') \tag{37}$$

where μ_{nl} denotes the eigenvalues of the RGM norm kernel:

$$\begin{aligned} \mu_{nl} =& \left\langle R_{nl}(r)\left[Y_l(\hat{r})\left[\Phi_{C_1}^{j_1\pi_1}\Phi_{C_2}^{j_2\pi_2}\right]_{j_{12}}\right]_J\right| \\ &\left.\mathcal{A}\left\{R_{nl}(r)\left[Y_l(\hat{r})\left[\Phi_{C_1}^{j_1\pi_1}\Phi_{C_2}^{j_2\pi_2}\right]_{j_{12}}\right]_J\right\}\right\rangle. \end{aligned} \tag{38}$$

Within the GCM–Brink framework, the coefficient e_{nl} can be calculated as [13]

$$\begin{aligned} e_{nl} =& (-)^{(n-l)/2}\sqrt{\frac{2l+1}{(n-l)!!(n+l+1)!!}} \\ &\sum_{pq}\frac{(\nu S_p^2)^{n/2}}{\sqrt{n!}}e^{-\nu S_p^2/2}B_{pq}^{-1}\left\langle \Phi_{j_1\pi_1j_2\pi_2j_{12}l}^{J\pi}(S_q)\middle|\Psi_{MA}^{J\pi}\right\rangle, \end{aligned} \tag{39}$$

where

$$B_{pq} = \left\langle \Phi^{J\pi}_{j_1\pi_1 j_2\pi_2 j_{12} l}(S_p) \middle| \Phi^{J\pi}_{j_1\pi_1 j_2\pi_2 j_{12} l}(S_q) \right\rangle, \tag{40}$$

$\Phi^{J\pi}_{j_1\pi_1 j_2\pi_2 j_{12} l}(S_p)$ is the Brink wave function projected onto the angular momenta and parities of the nucleus and the two clusters involved, and S_p is the discretized intercluster distance.

The traditional method for calculating the RWA using the GCM–Brink wave function requires significant computational resources. Recently, Chiba and Kimura [53] proposed a Laplace expansion method to calculate the RWA within the GCM/AMD framework. Through the Laplace expansion, the AMD wave function of the A-nucleon system, which is defined as the determinant of an $A \times A$ matrix $B_{A\times A}$, can be split into two AMD wave functions of clusters C_1 and C_2 ($A = C_1 + C_2$):

$$\Phi^{\rm AMD}_A = \sqrt{\frac{C_1!C_2!}{A!}} \sum_{1\le i_1<\cdots<i_{C_1}\le A} P(i_1,\cdots,i_{C_1}) \Phi^{\rm AMD}_{C_1}(i_1,\cdots,i_{C_1})\Phi^{\rm AMD}_{C_2}(i_{C_1+1},\cdots,i_A) \tag{41}$$

with a phase factor $P(i_1,\cdots,i_{C_1})$ defined as

$$P(i_1,\cdots,i_{C_1}) = (-)^{C_1(C_1+1)/2+\sum_{s=1}^{C_1} i_s}. \tag{42}$$

The cluster wave function $\Phi^{\rm AMD}_{C_1}(i_1,\cdots,i_{C_1})$ is defined as the determinant of the matrix composed of the $1,\cdots,C_1$th rows and the $i_1,\cdots,i_{C_1}$th columns of the matrix $B_{A\times A}$, and the determinant defining $\Phi^{\rm AMD}_{C_2}(i_{C_1+1},\cdots,i_A)$ consists of the elements that remain after removing the $1,\cdots,C_1$th rows and the $i_1,\cdots,i_{C_1}$th columns. The RWA can then be calculated as the sum of the coupling results of the three kernels with angular momentum and parity:

$$y^{J\pi}_{\rm c}(a) = \frac{1}{\sqrt{\mathcal{N}^{J\pi}_K}} \sum_{1\le i_1<\cdots<i_{C_1}\le A} P(i_1,\cdots,i_{C_1}) \times \left[\chi_l(a;i_1,\cdots,i_A) \otimes \left[N^{j_1\pi_1}(i_1,\cdots,i_{C_1}) \otimes N^{j_2\pi_2}(i_{C_1+1},\cdots,i_A)\right]_{j_{12}}\right]_{JK}, \tag{43}$$

in which

$$\chi_{lm_l}(a;i_1,\cdots,i_A) = \left\langle \frac{\delta(r-a)}{r^2} Y_{lm_l}(\hat{r}) \middle| \chi(\boldsymbol{r};i_1,\cdots,i_A) \right\rangle$$
$$N^{j_1\pi_1}_{m_1}(i_1,\cdots,i_{C_1}) = \left\langle \Phi^{j_1\pi_1}_{m_1 C_1} \middle| \Phi^{\rm int}_{C_1}(i_1,\cdots,i_{C_1}) \right\rangle$$
$$N^{j_2\pi_2}_{m_2}(i_{C_1+1},\cdots,i_A) = \left\langle \Phi^{j_2\pi_2}_{m_2 C_2} \middle| \Phi^{\rm int}_{C_2}(i_{C_1+1},\cdots,i_A) \right\rangle. \tag{44}$$

Note that the application of the Laplace expansion method to a symmetric clustering structure is time-consuming because the number of possible combinations for Laplace expansion increases when the system is heavy and the cluster mass number C_1 is close to C_2. In this case, traditional calculation methods can be applied more efficiently.

3.2 Asymptotic behavior

For cluster states in self-conjugated nuclei, such as $\alpha + \alpha$, as shown in Fig. 2, the RWA exhibits distinct features in different regions, namely suppressed inner oscillation, enhanced surface peak, and damping of the outer tail. The inner oscillation and enhanced peak are closely related to the antisymmetrization effect between the clusters. Due to the fermionic nature of the nucleons in the α clusters, the formation probability of the $\alpha + \alpha$ structure at a small distance is suppressed, and forbidden states appear at nodal distances. However, the tail part of the RWA, where the distance between clusters is sufficiently large that the antisymmetrization effect between clusters becomes very weak, is mainly determined by the separation energy as well as the

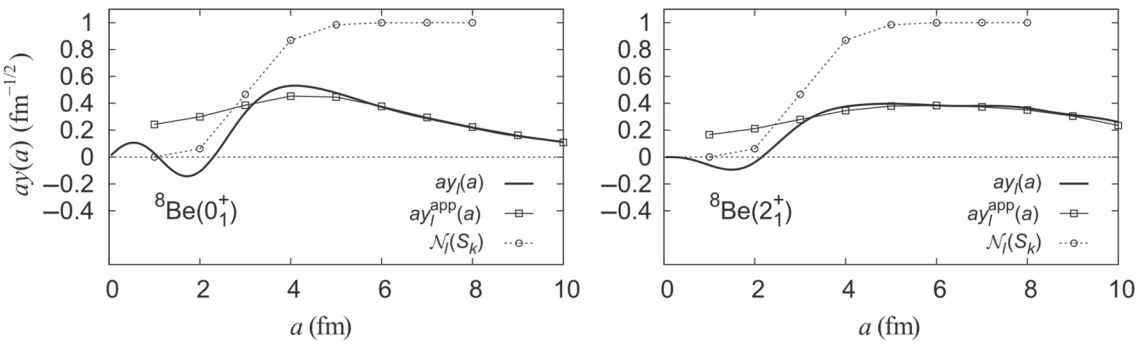

Fig. 2 (Color online) RWA and approximated RWA of the $\alpha + \alpha$ channel in 0^+_1 and 2^+_1 states of ^{8}Be. The figure is taken from Ref. [24]

centrifugal and Coulomb barriers. Consequently, the asymptotic behavior of the RWA should be well defined and is important for examining the delocalization of α clusters in weakly bound cluster states [54].

In addition, when nuclear reactions are analyzed, the asymptotic behavior of the RWA determines the angular distributions of the nucleon or cluster removal cross sections [27]. For bound systems and narrow resonances, the tail part of RWA decreases as

$$ay_{\rm c}^{J\pi}(a) \to C_{\rm c}^{J\pi} W_{-\eta,l+1/2}(2\kappa a), \tag{45}$$

where $W_{-\eta,l+1/2}(2\kappa a)$ is the Whittaker function, $\eta = Z_1 Z_2 e^2 \mu/\hbar^2\kappa$ is the Sommerfeld parameter, and $\kappa = \sqrt{-2\mu E}/\hbar$ is the wave number. $C_{\rm c}^{J\pi}$ is the asymptotic normalization coefficient, which plays an important role in reaction analyses.

The significance of the asymptotic behavior of RWA is further demonstrated by the consistency between the tail parts of the relative wave functions with distinctive definitions. It should be noted that the RWA is not normalized to unity but to $S_{\rm c}^2$ as shown in Eq. (21). If we define

$$u_l(r) = \sum_n e_n \sqrt{\mu_{nl}} R_{nl}(r), \tag{46}$$

it can be seen that, for the cluster model wave function normalized to unity (e.g., $\langle\Psi|\Psi\rangle = 1$), we have

$$\int |u_l(r)|^2 r^2 {\rm d}r = 1. \tag{47}$$

The difference between the relative wave functions $y_l(r)$, $u_l(r)$, and $\chi_l(r)$ is in the treatment of the antisymmetrization effect between clusters [24]. Based on Eq. (34), we can see that $\chi_l(r)$ is the cluster relative wave function before antisymmetrization and, as a result, contains nonphysical forbidden states whose norm kernel has an eigenvalue of $\mu_{nl} = 0$. By contrast, in the antisymmetrized relative wave functions $y_l(r)$ and $u_l(r)$, the forbidden-state components are eliminated by the coefficients μ_{nl} and $\sqrt{\mu_{nl}}$, respectively, whereas the treatments of the partially allowed states are different, and thus exhibit different normalization results. These distinctions can be inferred more explicitly by comparing Eqs. (37), (46), and (35). Notably, although the wave functions $\chi_l(r)$, $u_l(r)$, and $y_l(r)$ are different in the region in which the antisymmetrization effect plays a major role (i.e., the inner region with a small distance between clusters), they exhibit the same asymptotic behavior in the region with a large r, where the antisymmetrization effect is weak and can be ignored, i.e., for large r:

$$\chi_l(r) \approx y_l(r) \approx u_l(r). \tag{48}$$

Using this important feature, Kanada-En'yo et al. [24] showed that, for two-body cluster channels, the tail part of the RWA can be well approximated using the overlap of the cluster model wave function with the single-Brink wave function:

$$|ay_l(a)| \approx \frac{1}{\sqrt{2}}\left(\frac{2\nu'}{\pi}\right)^{1/4} \left|\left\langle \Psi_M^{J\pi} \middle| \Phi^{\rm B}(S=a)\right\rangle\right| \equiv a y^{\rm app}(a), \tag{49}$$

where S denotes the intercluster distance of the Brink wave function. In Fig. 2, we show both the approximated RWA and exact RWA of the 0_1^+ and 2_1^+ states of ^{8}Be. The approximated RWA describes the tail part well, although the inner oscillation is absent. As previously mentioned, when analyzing the decay characteristics, we need to examine only the RWA value for a relatively larger channel radius a. In this case, the approximation of RWA using a single-Brink overlap provides a practical calculation method that effectively reduces computational cost.

Testing the abilities of different trial wave functions is also interesting for describing the asymptotic behavior of the cluster relative motion. Based on the equivalence of the three types of relative wave function in the tail region, Kanada-En'yo [54] further calculated the relative wave functions obtained from the Brink, spherical THSR (sTHSR), and deformed THSR (dTHSR) wave functions as well as a function with Yukawa tail (YT) and compared them with the exact solution obtained by GCM wave function. The relative wave functions of these trail wave functions can be expressed as various types of Gaussians. For the Brink and sTHSR wave functions, the intercluster wave function can be adopted as a shifted spherical Gaussian (ssG)

$$\chi^{\rm ssG}(\boldsymbol{r}) = \exp\left[-\frac{(\boldsymbol{r}-\boldsymbol{S})^2}{\sigma^2}\right] \tag{50}$$

where the partial wave expansion is

$$\chi_l^{\rm ssG}(S,\sigma;r) \propto i_l\left(\frac{2Sr}{\sigma^2}\right) \exp\left(-\frac{r^2+S^2}{\sigma^2}\right), \tag{51}$$

where $i_l(r)$ is the regular modified spherical Bessel function. This function is controlled by two parameters, S and σ. When σ is fixed at $\sigma = 1/\sqrt{\nu'} = \sqrt{A/C_1C_2}b$, the relative wave function corresponds to the Brink wave function, whereas when $S \to 0$, the limit is equal to that of the sTHSR wave function. For the dTHSR wave function, the relative wave function is described by a deformed Gaussian (dG) function around the origin. If we consider the axially symmetric case as an example, then

$$\chi^{\mathrm{dG}}(\sigma_\perp,\sigma_z;\boldsymbol{r}) \propto \exp\left(-\frac{x^2}{\sigma_\perp^2}-\frac{y^2}{\sigma_\perp^2}-\frac{z^2}{\sigma_z^2}\right) = \exp\left(-\frac{r^2}{\sigma_\perp^2}+\frac{r^2}{\Delta}\cos\theta^2\right) \tag{52}$$

with

$$\frac{1}{\Delta} \equiv \frac{1}{\sigma_\perp^2}-\frac{1}{\sigma_z^2}. \tag{53}$$

For an even-l wave, the partial wave function can be calculated as

$$\chi_l^{\mathrm{dG}}(\sigma_\perp,\sigma_z;r) \propto 2\sqrt{(2l+1)\pi}\exp\left(-\frac{r^2}{\sigma_\perp^2}\right) \times \int_0^1 P_l(t)\exp\left(\frac{r^2}{\Delta}t^2\right)\mathrm{d}t, \tag{54}$$

and for an odd-l wave, we have

$$\chi_l^{\mathrm{dG}}(\sigma_\perp,\sigma_z;r) \propto 2\sqrt{(2l+1)\pi}r\exp\left(-\frac{r^2}{\sigma_\perp^2}\right) \times \int_0^1 P_l(t)t\exp\left(\frac{r^2}{\Delta}t^2\right)\mathrm{d}t, \tag{55}$$

where $P_l(t)$ is the Legendre polynomial.

To determine the accuracy of the trial wave functions in describing the asymptotic behavior of the cluster relative motions, Fig. 3 shows the relative wave function $ru_l(r)$ obtained by precise GCM solutions and trial wave functions that include the Brink, spherical, and deformed THSR, and Yukawa-type wave functions calculated by Kanada-En'yo [54]. For comparison, the results of the SM wave function are also shown. The results show that the SM and Brink wave functions can provide the correct number of oscillation nodes in the inner region. However, both decrease too quickly in the tail region to provide a reasonable asymptotic feature. In addition, the SM wave function exhibits an enhanced peak that is narrower and more inward than that of the precise wave function, whereas the Brink wave function shows a more outward peak. Notably, the Brink wave function reproduces the amplitudes of the inner oscillation part better and exhibits a longer tail than the SM wave function. However, the tail of the Brink relative wave function deviates significantly from the exact function because the Brink wave function is a localized model wave function. Introducing the nonlocalization character enables the sTHSR wave function to describe the relative wave function better than the Brink and SM wave functions, although minor deviations appear in the tail part. Surprisingly, the dTHSR and YT wave functions can generate very precise results for the cluster relative wave function, suggesting that they can serve as efficient trial wave functions in describing the relative motion between clusters.

3.3 Two-body overlap amplitude

The RWA is essentially a one-body overlap amplitude that depends on a single intercluster distance parameter. To observe the correlations between clusters or nucleons more clearly and to understand the much more complex three-body cluster motion, we can extend the analysis of overlap amplitudes to three-body channels. This extension was recently applied to the analysis of core + N + N structures [55–57]. Here, we provide a more general formula for

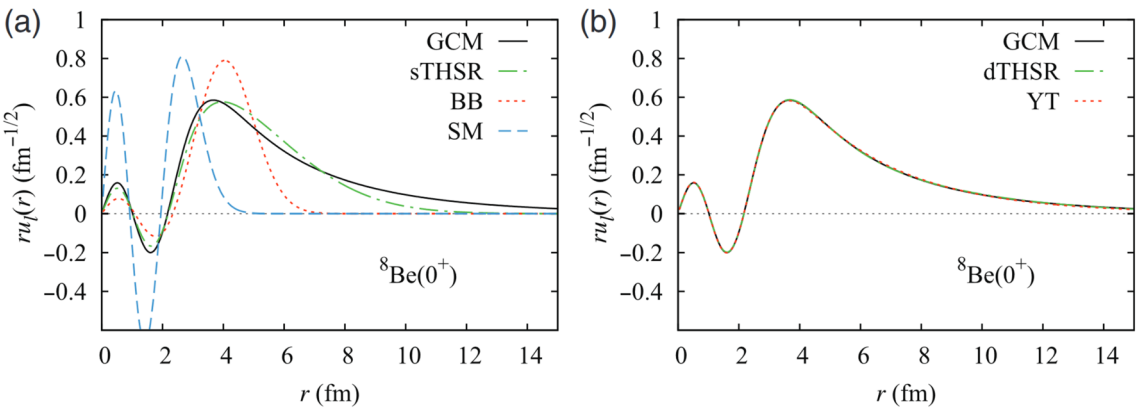

Fig. 3 (Color online) α-α cluster relative wave function obtained by GCM wave function of ^{8}Be(0$^+$), compared with that obtained by the shell model wave function, Brink wave function, spherical THSR wave function, deformed THSR wave function, and Yukawa tail function. The figure is taken from Ref. [54]

calculating the two-body overlap amplitude by iteratively applying the Laplace expansion method [53].

The two-body overlap amplitude is defined as

$$\mathcal{Y}_{\rm c}^{J\pi}(a_1,a_2)=\sqrt{\frac{A!}{C_1!C_2!C_3!}}\times\left\langle\frac{\delta(r_1-a_1)\delta(r_2-a_2)}{r_1^2r_2^2}\left[\left[Y_{l_1}(\hat{r}_1)\otimes Y_{l_2}(\hat{r}_2)\right]_L\otimes\left[\Phi_{C_1}^{j_1\pi_1}\otimes\left[\Phi_{C_2}^{j_2\pi_2}\otimes\Phi_{C_3}^{j_3\pi_3}\right]_{j_{23}}\right]_{j_{123}}\right]_{JM}\middle|\Psi_M^{J\pi}\right\rangle, \tag{56}$$

in which $c=\{j_1\pi_1j_2\pi_2j_3\pi_3j_{23}j_{123}l_1l_2L\}$ according to the three-body coupling channel of $[[C_1(j_1)\otimes[C_2(j_2)\otimes C_3(j_3)]_{j_{23}}]_{j_{123}}\otimes[l_1\otimes l_2]_L]_J$ and the parity relation of $\pi=(-)^{l_1+l_2}\pi_1\pi_2\pi_3$. The relative motion coordinates $\boldsymbol{r}_1$ and $\boldsymbol{r}_2$ are defined as follows.

$$\begin{aligned}\boldsymbol{r}_1&=\boldsymbol{X}_2-\boldsymbol{X}_3\\ \boldsymbol{r}_2&=\boldsymbol{X}_1-\frac{C_2\boldsymbol{X}_2+C_3\boldsymbol{X}_3}{C_2+C_3},\end{aligned} \tag{57}$$

where $\boldsymbol{X}_i$ is the COM of the physical coordinates of cluster C_i. By applying the Laplace expansion method twice to the AMD/Brink wave function, which is defined as a Slater determinant, we obtain

$$\Phi_A^{\rm AMD}=\sqrt{\frac{A!}{C_1!C_2!C_3!}}\sum_{\substack{1\le i_1<\cdots<i_{C_1}\le A\\ 1\le j_1<\cdots<j_{C_2}\le C_2+C_3}}P_A(i_1,\cdots,i_{C_1})P_{C_2+C_3}(j_1,\cdots,j_{C_2})\times\Phi_{C_1}^{\rm AMD}(i_1,\cdots,i_{C_1})\Phi_{C_2}^{\rm AMD}(j_1,\cdots,j_{C_2})\Phi_{C_3}^{\rm AMD}(j_{C_2+1},\cdots,j_{C_2+C_3}) \tag{58}$$

with the phase factor

$$\begin{aligned}P_A(i_1,\cdots,i_{C_1})&=(-)^{\frac{C_1(C_1+1)}{2}+\sum_s i_s}\\ P_{C_2+C_3}(j_1,\cdots,j_{C_2})&=(-)^{\frac{C_2(C_2+1)}{2}+\sum_s j_s}.\end{aligned} \tag{59}$$

Note that $j_s\,(s=1,\cdots,C_2+C_3)$ corresponds to the index in the matrix composed of the remaining elements after removing the rows and columns constituting $\Phi_{C_1}^{\rm AMD}$ from the matrix $B_{A\times A}$. Following the analogous procedure in the two-body Laplace expansion method calculation, the product of the three AMD wave functions can be rewritten as

$$\begin{aligned}&\Phi_{C_1}^{\rm AMD}\Phi_{C_2}^{\rm AMD}\Phi_{C_3}^{\rm AMD}\\ &=\Phi_{C_1}^{\rm cm}\Phi_{C_2}^{\rm cm}\Phi_{C_3}^{\rm cm}\Phi_{C_1}^{\rm int}\Phi_{C_2}^{\rm int}\Phi_{C_3}^{\rm int}\\ &=\left(\frac{C_1C_2C_3}{(\pi b^2)^3}\right)^{3/4}\exp\left\{-\frac{1}{2b^2}\left[C_1(\boldsymbol{X}_1-\boldsymbol{Z}_1)^2+C_2(\boldsymbol{X}_2-\boldsymbol{Z}_2)^2+C_3(\boldsymbol{X}_3-\boldsymbol{Z}_3)^2\right]\right\}\Phi_{C_1}^{\rm int}\Phi_{C_2}^{\rm int}\Phi_{C_3}^{\rm int}\\ &=\left(\frac{C_1C_2C_3}{(\pi b^2)^3}\right)^{3/4}\exp\left\{-\frac{1}{2b^2}\left[AX_G^2+\frac{C_2C_3}{C_2+C_3}(\boldsymbol{r}_1-\boldsymbol{S}_1)^2+\frac{C_1(C_2+C_3)}{C_1+C_2+C_3}(\boldsymbol{r}_2-\boldsymbol{S}_2)^2\right]\right\}\Phi_{C_1}^{\rm int}\Phi_{C_2}^{\rm int}\Phi_{C_3}^{\rm int}\\ &=\Phi_A^{\rm cm}\chi_{23}(\boldsymbol{r}_1)\chi_{123}(\boldsymbol{r}_2)\Phi_{C_1}^{\rm int}\Phi_{C_2}^{\rm int}\Phi_{C_3}^{\rm int},\end{aligned} \tag{60}$$

where $\boldsymbol{Z}_i$ is the COM of the generator coordinates of the nucleons in cluster C_i, and $\boldsymbol{S}_i$ is the corresponding Jacobi coordinate.

$$\Phi_A^{\rm cm} = \left(\frac{A}{\pi b^2}\right)^{3/4} \exp\left[-\frac{A}{2b^2}X_G^2\right] \tag{61}$$

is the COM wave function of the nucleus, and

$$\begin{aligned}
\chi_{23}(\boldsymbol{r}_1) &= \left(\frac{C_2C_3}{C_2+C_3}\frac{1}{\pi b^2}\right)^{3/4} \\
&\quad \exp\left[-\frac{C_2C_3}{C_2+C_3}\frac{1}{2b^2}(\boldsymbol{r}_1-\boldsymbol{S}_1)^2\right] \\
\chi_{123}(\boldsymbol{r}_2) &= \left(\frac{C_1(C_2+C_3)}{A}\frac{1}{\pi b^2}\right)^{3/4} \\
&\quad \exp\left[-\frac{C_1(C_2+C_3)}{A}\frac{1}{2b^2}(\boldsymbol{r}_2-\boldsymbol{S}_2)^2\right]
\end{aligned} \tag{62}$$

are the relative wave functions between C_2 and C_3 and between C_1 and the COM of C_2+C_3, respectively. $\Phi^{\rm int}_{C_1}$, $\Phi^{\rm int}_{C_2}$, and $\Phi^{\rm int}_{C_3}$ are the intrinsic wave functions of C_1, C_2, and C_3. Then, the two-body overlap amplitude can be calculated by

$$\begin{aligned}
&\mathcal{Y}_{\rm c}^{J\pi}(a_1,a_2) \\
&= \sqrt{\frac{A!}{C_1!C_2!C_3!}}\left\langle \frac{\delta(r_1-a_1)\delta(r_2-a_2)}{r_1^2r_2^2} \right. \\
&\quad \left. \left[\left[Y_{l_1}(\hat{r}_1)\otimes Y_{l_2}(\hat{r}_2)\right]_L \otimes \left[\Phi^{j_1\pi_1}_{C_1}\otimes\left[\Phi^{j_2\pi_2}_{C_2}\otimes\Phi^{j_3\pi_3}_{C_3}\right]_{j_{23}}\right]_{j_{123}}\right]_{JM} \middle| \Psi^{J\pi}_M \right\rangle \\
&= \sqrt{\frac{A!}{C_1!C_2!C_3!}}\left\langle \frac{\delta(r_1-a_1)\delta(r_2-a_2)}{r_1^2r_2^2}P^{J\pi}_{KM} \right. \\
&\quad \left. \left[\left[Y_{l_1}(\hat{r}_1)\otimes Y_{l_2}(\hat{r}_2)\right]_L \otimes \left[\Phi^{j_1\pi_1}_{C_1}\otimes\left[\Phi^{j_2\pi_2}_{C_2}\otimes\Phi^{j_3\pi_3}_{C_3}\right]_{j_{23}}\right]_{j_{123}}\right]_{JM} \middle| \Psi^{\rm int}_A \right\rangle \\
&= \sqrt{\frac{A!}{C_1!C_2!C_3!}}\left\langle \frac{\delta(r_1-a_1)\delta(r_2-a_2)}{r_1^2r_2^2} \right. \\
&\quad \left. \left[\left[Y_{l_1}(\hat{r}_1)\otimes Y_{l_2}(\hat{r}_2)\right]_L \otimes \left[\Phi^{j_1\pi_1}_{C_1}\otimes\left[\Phi^{j_2\pi_2}_{C_2}\otimes\Phi^{j_3\pi_3}_{C_3}\right]_{j_{23}}\right]_{j_{123}}\right]_{JK} \middle| \Psi^{\rm int}_A \right\rangle \\
&= \frac{1}{\sqrt{\mathcal{N}^{J\pi}_K}} \sum_{\substack{1\le i_1<\cdots<i_{C_1}\le A \\ 1\le j_1<\cdots<j_{C_2}\le C_2+C_3}} P_A(i_1,\cdots,i_{C_1})P_{C_2+C_3}(j_1,\cdots,j_{C_2}) \\
&\quad \times\left[\left[\chi^{23}_{l_1}\otimes\chi^{123}_{l_2}\right]_L\otimes\left[N^{j_1\pi_1}(i_1,\cdots,i_{C_1})\otimes\left[N^{j_2\pi_2}(j_1,\cdots,j_{C_2})\otimes N^{j_3\pi_3}(j_{C_2+1},\cdots,j_{C_2+C_3})\right]_{j_{23}}\right]_{j_{123}}\right]_{JK}
\end{aligned} \tag{63}$$

with the overlap kernels defined as

$$\begin{aligned}
&\chi^{23}_{l_1m_{l1}}(a_1;j_1,\cdots,j_{C_2+C_3}) \\
&\quad = \left\langle \frac{\delta(r_1-a_1)}{r_1^2}Y_{l_1m_{l1}}(\hat{r}_1)\middle|\chi^{23}(\boldsymbol{r}_1;j_1,\cdots,j_{C_2+C_3})\right\rangle \\
&\chi^{123}_{l_2m_{l2}}(a_2;i_1,\cdots,i_{C_1},j_1,\cdots,j_{C_2+C_3}) \\
&\quad = \left\langle \frac{\delta(r_2-a_2)}{r_2^2}Y_{l_2m_{l2}}(\hat{r}_2)\middle|\chi^{123}(\boldsymbol{r}_2;i_1,\cdots,i_{C_1},j_1,\cdots,j_{C_2+C_3})\right\rangle \\
&N^{j_1\pi_1}_{m_1}(i_1,\cdots,i_{C_1}) \\
&\quad = \left\langle \Psi^{j_1\pi_1}_{m_1C_1}\middle|\Phi^{\rm int}_{C_1}(i_1,\cdots,i_{C_1})\right\rangle \\
&N^{j_2\pi_2}_{m_2}(j_1,\cdots,j_{C_2}) \\
&\quad = \left\langle \Psi^{j_2\pi_2}_{m_2C_2}\middle|\Phi^{\rm int}_{C_2}(j_1,\cdots,j_{C_2})\right\rangle \\
&N^{j_3\pi_3}_{m_3}(j_{C_2+1},\cdots,j_{C_2+C_3}) \\
&\quad = \left\langle \Psi^{j_3\pi_3}_{m_3C_3}\middle|\Phi^{\rm int}_{C_3}(j_{C_2+1},\cdots,j_{C_2+C_3})\right\rangle.
\end{aligned} \tag{64}$$

4 Applications

The RWA (or cluster form factor in NCSM formalism or overlap function in reaction theories) has been extensively applied in a wide range of studies. In addition to its ability to analyze cluster configurations and calculate reaction cross sections, the RWA (cluster form factor) also serves as an indispensable quantity for solving the equation of motion in the no-core shell model with continuum (NCSMC), which is an *ab initio* theory that combines the NCSM with the cluster model [58, 59].

As Fig. 4 shows, the RWA calculated by the GCM and NCSMC [60] are compared for the $\alpha + {}^3$He structure in the ground and first excited states of ^{7}Be. We can see that despite different model wave functions and interactions adopted, the results obtained by NCSMC are basically consistent with those obtained by GCM, particularly for the tail part. In addition, the positions of the nodes that correspond to the forbidden states predicted by these two theoretical models agree well with each other. The main distinction between the results is that compared with those obtained from GCM, the NCSMC results exhibit higher inner peaks and more inward surface peaks.

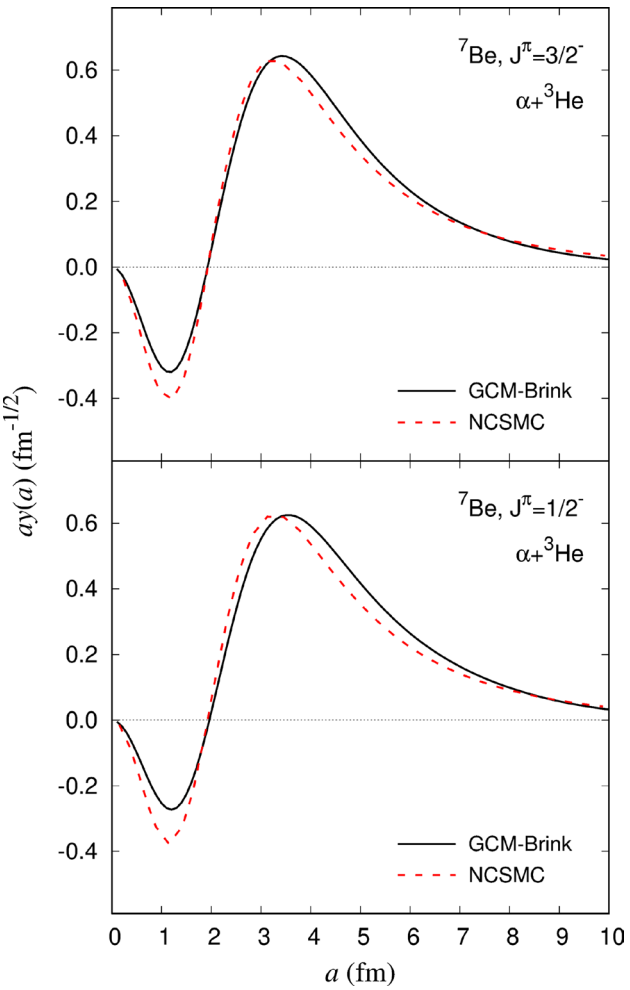

Fig. 4 (Color online) $\alpha + {}^3$He RWA for $3/2^-$ and $1/2^-$ states of ^{7}Be calculated by GCM and NCSMC [60]

In this article, we review the theory and applications of RWA in nuclear clustering studies. In the following section, we demonstrate the application of RWA to the clustering structural analysis based on cluster model wave functions. Some reaction studies closely related to clustering structures in the nuclei and the calculation of RWA are also briefly discussed.

4.1 Clustering structure in $N\alpha$ nuclei

One of the most interesting phenomena related to clustering in nuclei is the existence of the Hoyle state and its analogs in $N\alpha$ self-conjugate nuclei, in which α clusters simultaneously occupy the lowest 0^+ state and present the characteristic of BEC [19]. The Hoyle state is essential for the evolution of life because it plays a crucial role in the nucleosynthesis of isotopes heavier than helium [20, 61]. However, the structural configuration of the Hoyle state has been debatable since its discovery [62–64]. The subsequent discussion reveals that the RWA is an effective tool for searching and verifying $N\alpha$-condensation states in light nuclei.

By means of $\alpha + \alpha + \alpha$ GCM, Uegaki et al. [65] systematically calculated the ground and excited states of ^{12}C. To study the coupling between the α cluster and ^{8}Be in the ground and excited states, the RWA of various $^8\text{Be} + \alpha$ channels were evaluated for the obtained states of ^{12}C. We found that the Hoyle state 0_2^+ was predominantly composed of the channel $[^8\text{Be}(0^+) \otimes \alpha]_0 \otimes 0$. Because ^{8}Be is a well-known weakly bound nucleus, Uegaki et al. concluded that the Hoyle state is constructed by the weak coupling of ^{8}Be and α clusters or, equivalently, three α clusters, suggesting that all three α clusters occupy the lowest $0S$ orbit and form a gas-like state. This result was later confirmed in studies on the Hoyle state [66, 67]. In Fig. 5, we present our results of the RWA for various $^8\text{Be} + \alpha$ channels in $0_{1,2}^+$ and $2_{1,2}^+$ states of ^{12}C obtained using the GCM. For the lowest two states, 0_1^+ and 2_1^+, the clustering structures contained more than one channel with comparable amplitudes and similar curve structures. This characteristic suggests a more pronounced shell model structure of these two states due to a mixture of multiple cluster configurations along with typical inner oscillations and short tails. By contrast, the 0_2^+ and 2_2^+ states exhibit more significant clustering features. As noted by Uegaki et al., the RWA of the $[^8\text{Be}(0^+) \otimes \alpha]_0 \otimes 0$ channel in the 0_2^+ state is significantly enhanced in terms of amplitude. The outward-shifted peak also matches the larger radius of the Hoyle state. The clustering structure of the 2_2^+ state is more complicated and dominated by the $[^8\text{Be}(2^+) \otimes \alpha]_0 \otimes 0$

and $[^8\mathrm{Be}(0^+) \otimes \alpha]_0 \otimes 2$ channels in the interior and exterior regions, respectively. More recently, 0^+ states higher than the Hoyle state were reanalyzed using the THSR wave function to search for correlations between α clusters [68]. By calculating the $[^8\mathrm{Be}(0^+) \otimes \alpha]_0 \otimes 0$ RWA, as shown in Fig. 6, the 0_3^+ state is recognized as a breathing-like excited state of the Hoyle state because it exhibits a very extended amplitude and one more node than the Hoyle state in the RWA. On the other hand, the 0_4^+ state is considered to be a possible bent-arm-structure state with a significantly suppressed $[^8\mathrm{Be}(0^+) \otimes \alpha]_0 \otimes 0$ amplitude in the RWA.

Although the 4α condensate state of ^{16}O has been predicted using gas-like THSR wave functions [19], the identification of this state has been controversial for years. With the semi-microscopic method OCM, Funaki et al. [70] reproduced the full experimental spectrum of 0^+ states for ^{16}O up to 0_6^+ (denoted as $(0_6^+)_{\mathrm{OCM}}$ hereafter). They also provided the RWA results of various channels for the $(0_6^+)_{\mathrm{OCM}}$ state, which was considered in that work as a strong candidate for the Hoyle-analog 4α condensate state. The calculated RWA clearly shows that the obtained $(0_6^+)_{\mathrm{OCM}}$ state is predominantly composed of a $[^{12}\mathrm{C}(0_2^+) \otimes \alpha]_0 \otimes 0$ channel with an extended tail, whereas the ground state is dominated by a channel with $^{12}\mathrm{C}(0_1^+)$ and shows a steep tail decrease. Later, the same authors [69] more elaborately analyzed the 0^+ states of ^{16}O by employing THSR wave functions. Interestingly, in that study, the state with characteristics consistent with the $(0_6^+)_{\mathrm{OCM}}$ state, including the resonance energy, RMS radius, and $M(E0)$ transition strength, was identified as the fourth 0^+ state and is denoted as $(0_4^+)_{\mathrm{THSR}}$. The correspondence between the structures of the two theoretically obtained states was confirmed by comparing the RWA results. The RWA of $\alpha + ^{12}$C configurations calculated for $(0_4^+)_{\mathrm{THSR}}$ (Fig. 7) exhibited features similar to those of $(0_6^+)_{\mathrm{OCM}}$. The reason for the scarcity of states obtained by the THSR method can be understood by considering that complex channels involving higher angular momentum or negative-parity states of ^{12}C were not included in the early version of the THSR wave function, which was designed to describe gas-like structures.

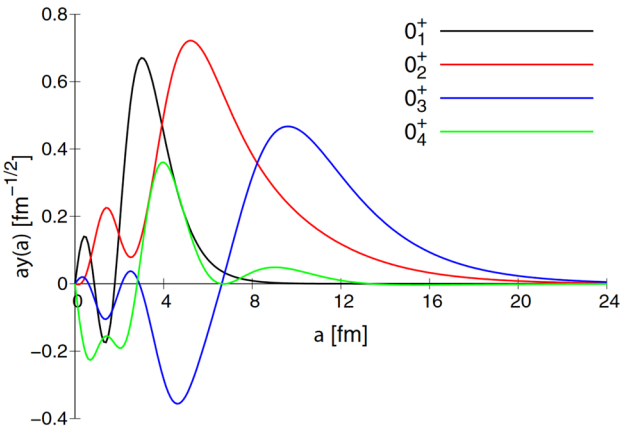

Fig. 6 (Color online) RWA of the $[^8\mathrm{Be}(0^+) \otimes \alpha]_0 \otimes 0$ channel in the 0_1^+, 0_2^+, 0_3^+, and 0_4^+ states of ^{12}C. The figure is taken from Ref. [68]

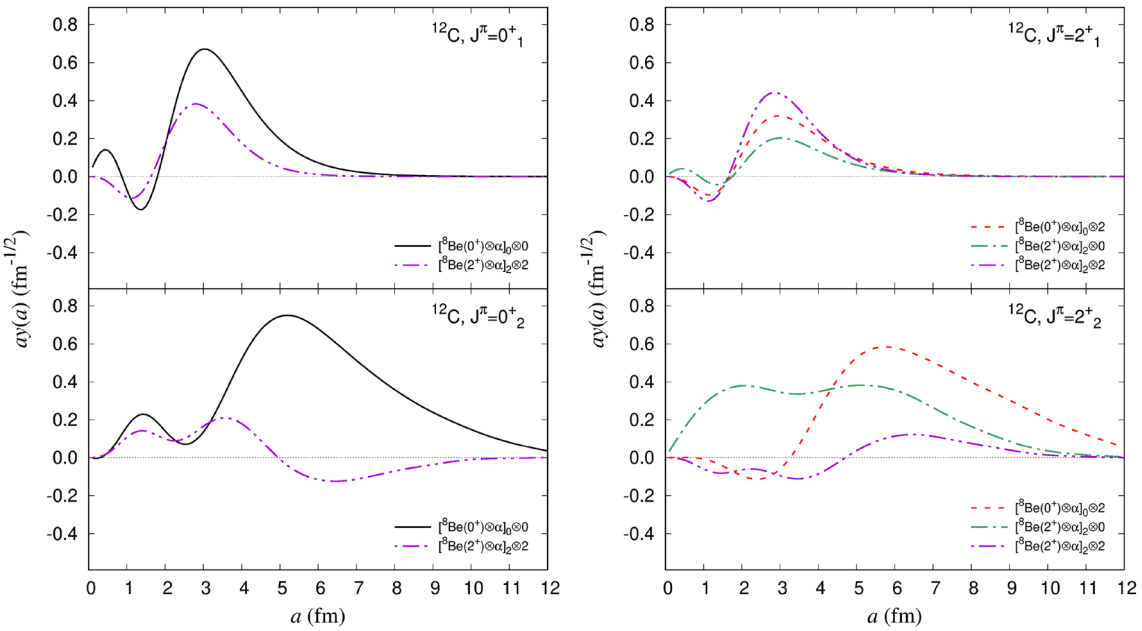

Fig. 5 (Color online) Calculated RWAs for various $^8\mathrm{Be} + \alpha$ channels in 0_1^+, 0_2^+, 2_1^+, and 2_2^+ states of ^{12}C

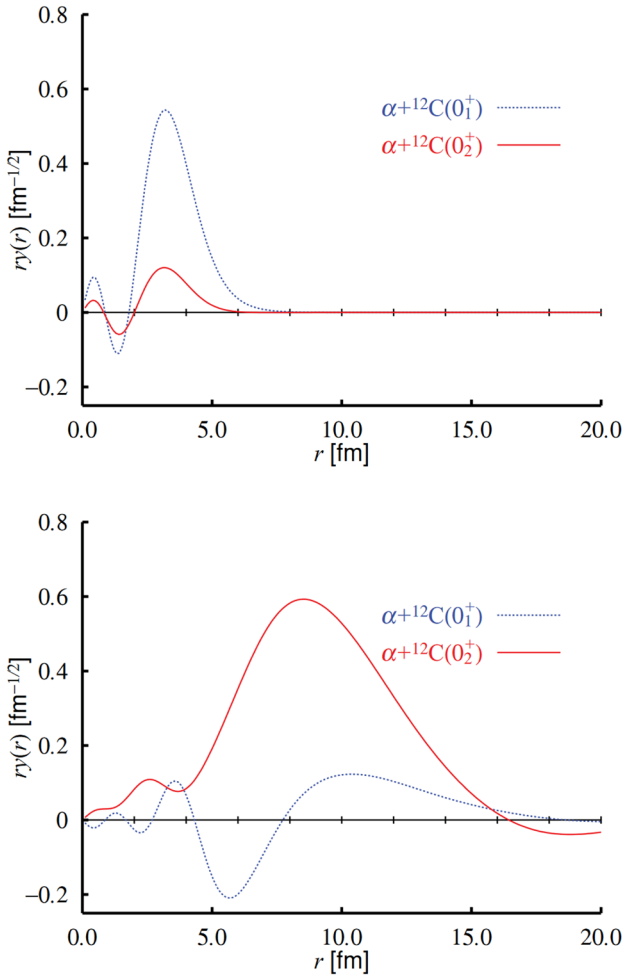

Fig. 7 (Color online) RWA of the $[^{12}C(0^+_{1,2}) \otimes \alpha]_0 \otimes 0$ channel in the 0^+_1 and 0^+_4 states of ^{16}O obtained by THSR calculation. The figure is taken from Ref. [69]

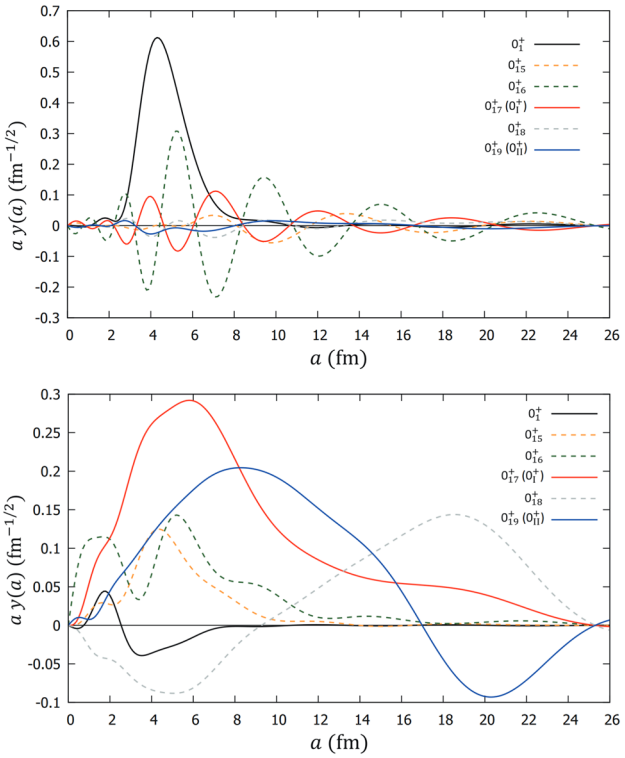

Fig. 8 (Color online) RWAs of the $[^{16}O(0^+_1) \otimes \alpha]_0 \otimes 0$ and $[^{16}O(0^+_6) \otimes \alpha]_0 \otimes 0$ channels in ground and excited states above the 5α threshold of ^{20}Ne. The figure is taken from Ref. [71]

Consisting of five α clusters, the relative motions between the clusters in ^{20}Ne are more complicated. By calculating the $^{16}O + \alpha$ RWA for various rotational bands of ^{20}Ne, Kimura [72] investigated the relative motions of ^{16}O and α clusters. Similar to ^{12}C and ^{16}O, for the low-lying states of ^{20}Ne, the RWA results of various $^{16}O + \alpha$ components oscillate and are suppressed in the interior region, and are then clearly enhanced in the exterior region. The calculated RWA also demonstrated that the ground band of ^{20}Ne exhibits a pronounced anti-stretching phenomenon because the average distance between the ^{16}O and α clusters decreases as the angular momentum increases. The 5α condensate state is predicted to be much higher, at approximately 20 MeV, making the search for this state much more difficult. Recently, Zhou et al. [71] theoretically recognized the 5α condensate state of ^{20}Ne at 2.7 MeV above the 5α threshold. The calculated RWA shows that, analogous to the 3α and 4α condensate states, the 5α condensate state (denoted as 0^+_I) is dominated by the $[^{16}O(0^+_6) \otimes \alpha]_0 \otimes 0$ channel with features of an enhanced and extended amplitude and zero node, as depicted in Fig. 8. In addition, another higher 0^+ state, denoted as 0^+_{II}, was also found to possess a significant $[^{16}O(0^+_6) \otimes \alpha]_0 \otimes 0$ component, but with one node in the RWA. The enhanced monopole transition between 0^+_I and 0^+_{II} as well as the nodal structures of the RWA suggests that the 0^+_{II} state is a breathing-like excitation of the 5α condensate state.

4.2 Clustering in neutron-rich nuclei

In addition to the Hoyle and Hoyle-analog states in $N\alpha$ nuclei, neutron-rich nuclei exhibit various interesting cluster states [73]. Since the 1990s, both experimental [74] and theoretical studies [75–77] have suggested that a novel form of clustering via the molecular structure may occur in neutron-rich Be or C isotopes, in which the α clusters interact with extra neutrons, serving as valence neutrons akin to covalent electrons that bind atoms in a molecule.

One of the simplest examples of a molecular state is ^9Be, in which the unbound system of $\alpha + \alpha$ is bound by the addition of one valence neutron. By combining the resonant state

method with the RGM, Arai et al. [78] systematically studied the structure of the ground and excited states of ^{9}Be and calculated the ^{8}Be + n and ^{5}He + α RWAs for some low-lying states, including $3/2^-$, $5/2^-$, $1/2^+$, $1/2^-$, and $5/2^+$. The results show that in these states, both the ^{8}Be + n and ^{5}He + α configurations exhibit large amplitudes. In addition, the maximum amplitude is reached with a larger distance between clusters for positive-parity states than for negative-parity states, suggesting that the average α–α distances in positive-parity states are larger, consistent with earlier studies [79].

More structural information, besides the binary clustering probability, can be inferred from the RWA of neutron-rich nuclei. For example, the orbits of valence neutrons were analyzed in a groundbreaking study [81] on the molecular states in ^{12}Be. By examining the RWA of different rotational bands in ^{6}He + ^{6}He and ^{8}He + α systems and considering molecular orbits of neutrons, Kanada-En'yo and Horiuchi concluded that in the $K^\pi = 0_1^+$ band, the neutrons surround a core composed of the two α clusters, as indicated by the significant ^{6}He + ^{6}He and ^{8}He + α RWA in these states. By contrast, the neutrons move around either one of the α clusters in the $K^\pi = 0_3^+$ band, provided that only the ^{6}He + ^{6}He structure dominates these states.

Furthermore, RWA analysis allows for an investigation of the tendency of α clustering as the drip-line is approached. A recent experiment demonstrated a negative correlation between α formation and neutron skin thickness in Sn isotopes [10]. Following this, α cluster formation in neutron-rich isotopes of Be and B was systematically analyzed by calculating the RWA of $\alpha + {}^{X-4}$He structures [82]. The study found that, although the α RWA decreased as the neutron number increased, the overall cluster formation probability was still enhanced. This was because the structures consisting of neutron-rich clusters, such as ^{6}He + ^{6}He in ^{12}Be and ^{6}He + ^{8}He in ^{14}Be, became comparable with the α-clustering structures.

A similar relationship between α formation on the nuclear surface and the richness of neutrons has also been studied for C isotopes [80]. In that study, the RWAs of various $\alpha + {}^{X-4}$Be channels were calculated for the ground states of ^{14}C, ^{16}C, and ^{18}C, as shown in Fig 9. The results showed that for ^{14}C, the α amplitude in the exterior was large and comparable with that for ^{12}C, whereas for ^{16}C and ^{18}C, with thicker neutron skins, the α formation on the nuclear surface was considerably suppressed.

The formation of exotic clusters, other than α clusters, in neutron-rich nuclei has attracted increasing attention. Through the use of RWA, the formation probabilities of not only α clusters but also light exotic clusters such as triton, ^{3}He, and deuterons, etc., can be theoretically estimated. More significantly, another type of Hoyle-analog state, composed of different types of clusters forming gas-like states, has been proposed as existing among these exotic clustering states.

A natural candidate for searching for non-$N\alpha$ Hoyle-analog states is ^{11}B, which can be well described by the $\alpha + \alpha + $t cluster model. By means of AMD, Kanada-En'yo [84] found that the $3/2_3^-$ state of ^{11}B is characterized by a dilute density distribution similar to that of the Hoyle state. Yamada and Funaki [85] later showed that the essence of the Hoyle-analog state lies in the occupancy of the lowest $0S$ orbit for all constituent clusters, thus avoiding the Pauli blocking effect among them to form a gas-like configuration. Using OCM calculations, they demonstrated that the $1/2_2^+$ state of ^{11}B is a strong candidate for the Hoyle-analog state of $\alpha + \alpha + $t clustering. Thus, due to the lack of experimental results, the identification of the Hoyle-analog state in ^{11}B remains controversial. Recent GCM calculation results of ^{11}B [86] support the gas-like nature of the $3/2_3^-$ state but are quite different in the description of the $1/2_2^+$ state, indicating that it exhibits a linear chain-like structure.

Adding an extra nucleon to the Hoyle state is another approach for exploring non-$N\alpha$ Hoyle-analog states. The configurations of $^{12}\mathrm{C}(0_2^+) + $n for ^{13}C were analyzed using the OCM [87] and AMD [83], and their predictions of the Hoyle-analog state were consistently $1/2_2^+$. The RWAs obtained from AMD calculations are presented in Fig. 10, which shows that the $[^{12}\mathrm{C}(0_2^+) \otimes \mathrm{n}]_{1/2} \otimes 0$ channel is predominant in the $1/2_2^+$ state, whereas the other $1/2^+$ states exhibit multichannel configurations. The SFs of various ^{12}C + n and ^{9}Be + α channels are shown in Fig. 11, where an obvious enhancement in the $[^{12}\mathrm{C}(0_2^+) \otimes \mathrm{n}]_{1/2} \otimes 0$ SF can be observed.

For certain high-lying states of light nuclei, the α cluster may interact with loosely bound valence nucleons to form various exotic clustering structures. With the ^{7}Li used as an example, although the most well-known clustering structure of $\alpha + $t in ^{7}Li has been extensively studied for decades [88–90], the core + N configurations, including ^{6}Li + n and ^{6}He + p, also constitute significant components in the ground state and even dominate in some highly excited states. More importantly, these higher-lying states related to the ^{6}He or ^{6}Li channels may play a role in the production and destruction of ^{7}Li in the early Universe, which is closely associated with unsolved cosmological lithium problems [91]. Here, we calculated the RWAs of various channels for some states of ^{7}Li to demonstrate the variety of clustering configurations with increasing excitation energy. The results are shown in Fig. 12.

From the results, we can clearly observe the multichannel character of the cluster configurations in the two bound states: the ground state $3/2^-$ and first excited state $1/2^-$. In these two states, in addition to the dominant $\alpha + $t configuration, the ^{6}He + p and various ^{6}Li + n channels exhibit significant amplitudes. This characteristic may correspond

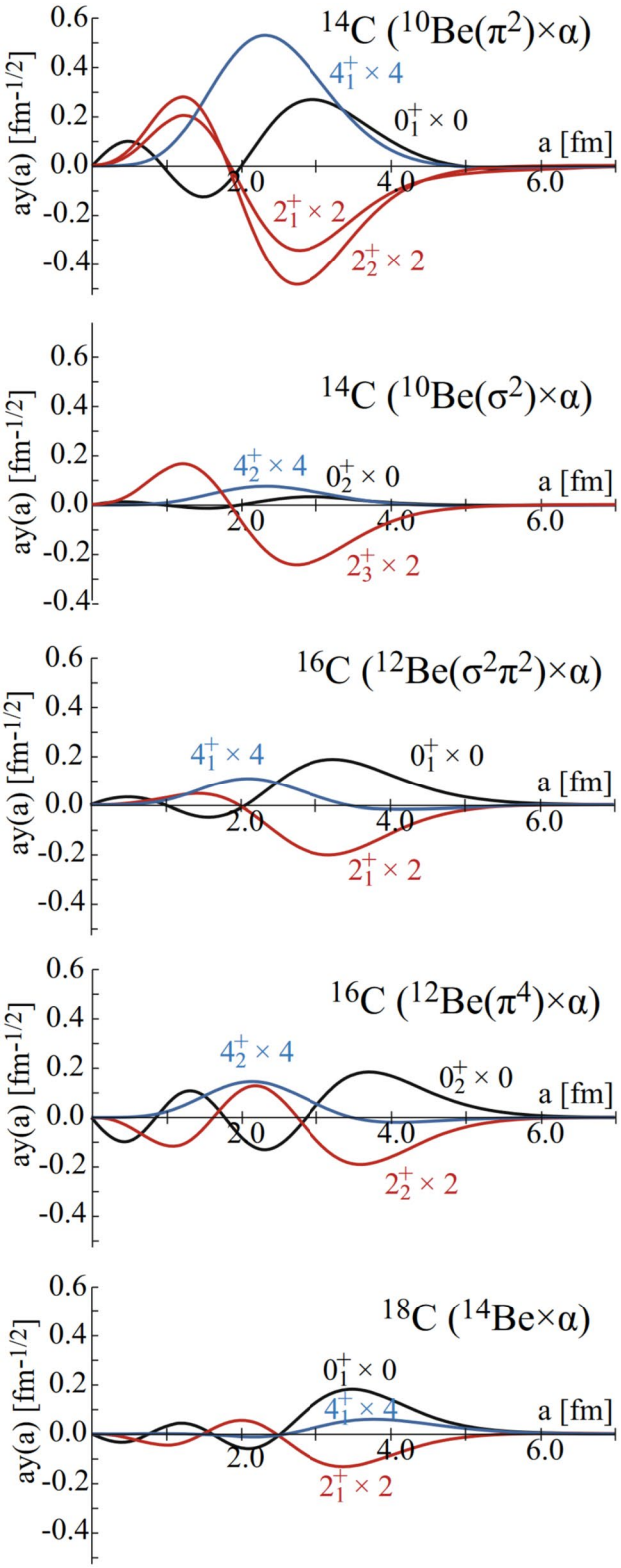

Fig. 9 (Color online) RWAs of $^{X-4}$Be + α channels in ground states of ^{14}C, ^{16}C, and ^{18}C. The figure is taken from Ref. [80]

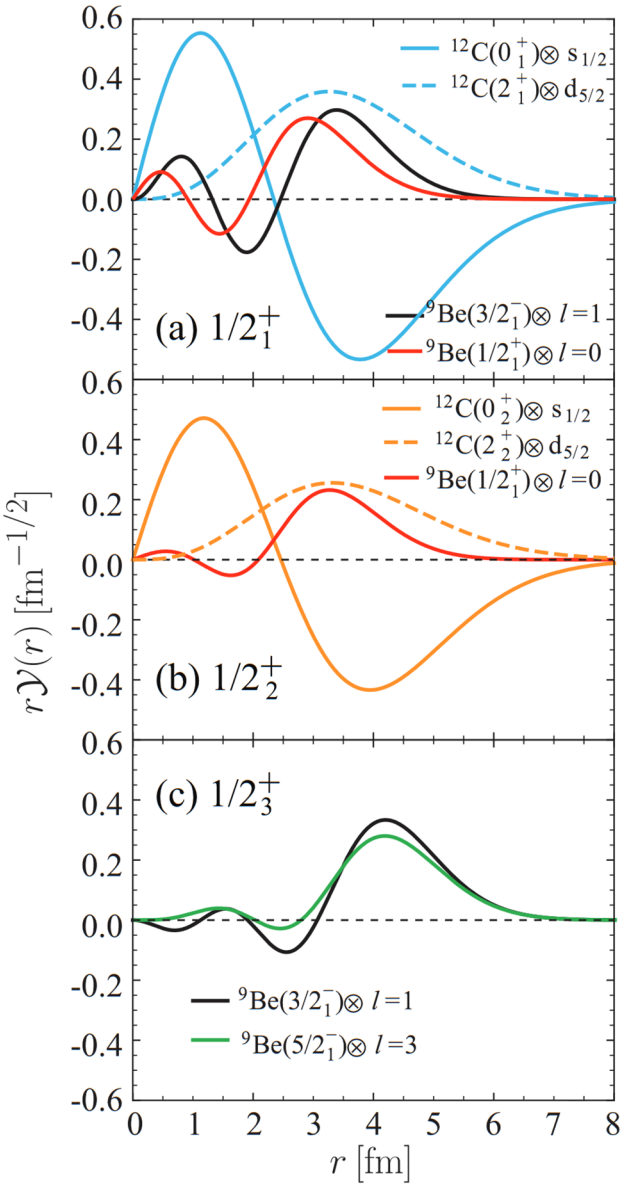

Fig. 10 (Color online) RWAs of various ^{12}C + n and ^{9}Be + α channels in $1/2^+_1$, $1/2^+_2$, and $1/2^+_3$ states of ^{13}C. The figure is taken from Ref. [83]

to a mixture of pronounced α + t clustering and moderate shell model configurations. On the other hand, the resultant RWA shows that in the two high-lying resonant states above the α + n + n + p threshold, $3/2^-_3$ and $3/2^-_4$, the α + t amplitude is significantly suppressed, particularly for the higher $3/2^-_4$ state. By contrast, the core + N configurations, both the ^{6}He + p and ^{6}Li + n structures, become the dominant binary clustering structures.

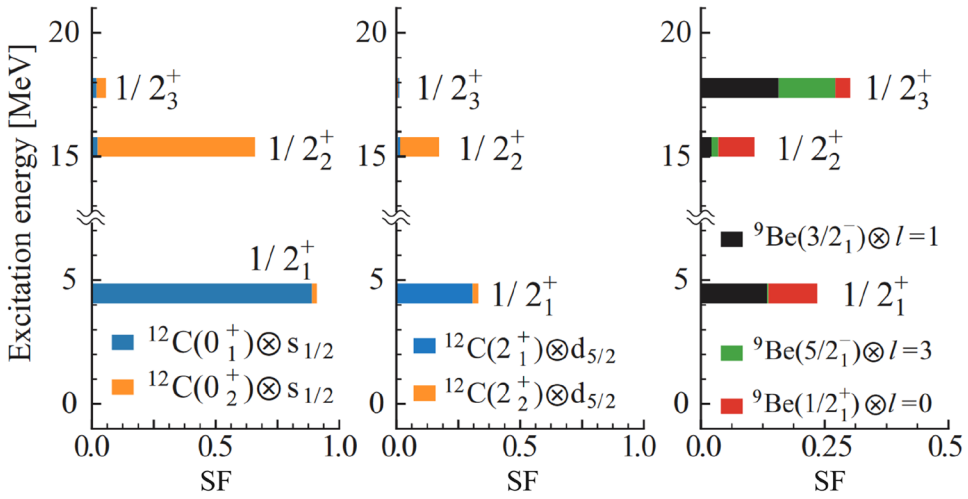

Fig. 11 (Color online) SFs of the ^{12}C + n and ^{9}Be + α channels in the $1/2^+_1$, $1/2^+_2$, and $1/2^+_3$ states of ^{13}C. The figure is taken from Ref. [83]

4.3 Analysis of three-body correlations

Recently, correlations between clusters or nucleons have drawn increasing interest [92, 93] and require an analysis of the three-body motions of clusters.

The motion of the two valence neutrons around the core is closely related to the well-known di-neutron correlation [94], which is fundamental for a deeper understanding of the nuclear force. Based on the framework presented in Sec. 3.3, as examples, the two-body overlap amplitudes of the ground states of ^{6}He and ^{10}Be are calculated, depicting the relative motions for α + n + n and ^{8}Be + n + n clustering structures, respectively. From the results, the motions and correlations of the two valence neutrons outside the core are clearly demonstrated, where r_1 denotes the distance between the two valence neutrons and r_2 is the distance from the core to the COM of the two valence neutrons.

Figure 13 shows the two-body overlap amplitude of the $[\alpha \otimes [\mathrm{n} \otimes \mathrm{n}]_0]_0 \otimes [0 \otimes 0]_0$ configuration for ^{6}He. The results exhibit two well-developed peaks located at $(r_1 = 4.4\ \mathrm{fm}, r_2 = 1.1\ \mathrm{fm})$ and $(r_1 = 2.1\ \mathrm{fm}, r_2 = 3.0\ \mathrm{fm})$, respectively. The peak at $(r_1 = 2.1\ \mathrm{fm}, r_2 = 3.0\ \mathrm{fm})$ represents a stronger correlation between the two valence neutrons than between the valence neutron and α core, which is always recognized as the di-neutron configuration. However, the smaller peak at $(r_1 = 4.4\ \mathrm{fm}, r_2 = 1.1\ \mathrm{fm})$ is associated

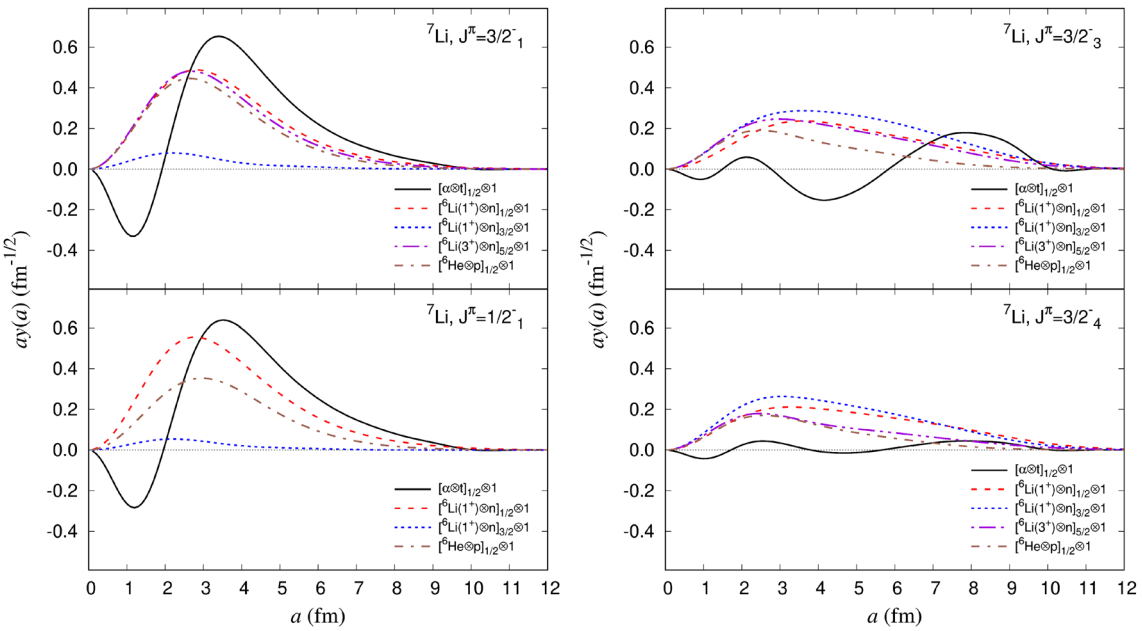

Fig. 12 (Color online) Calculated RWAs of the α + t, ^{6}Li + n, and ^{6}He + p channels in the $3/2^-_1$, $1/2^-_1$, $3/2^-_3$, and $3/2^-_4$ states of ^{7}Li

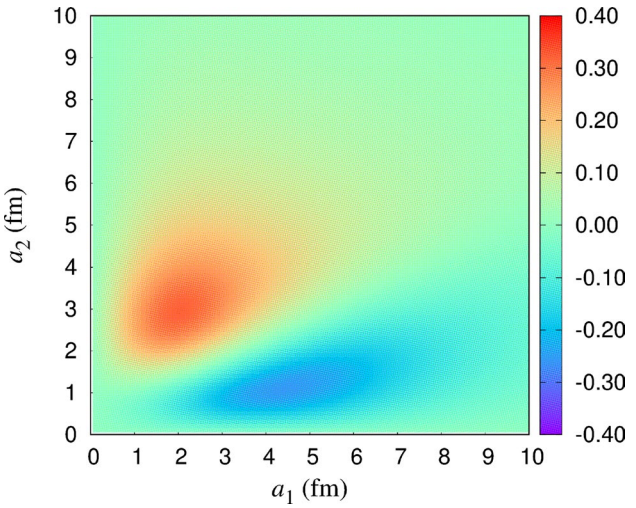

Fig. 13 (Color online) Calculated two-body overlap amplitude of the $[\alpha \otimes [\mathrm{n} \otimes \mathrm{n}]_0]_0 \otimes [0 \otimes 0]_0$ channel in the ground state of ^{6}He

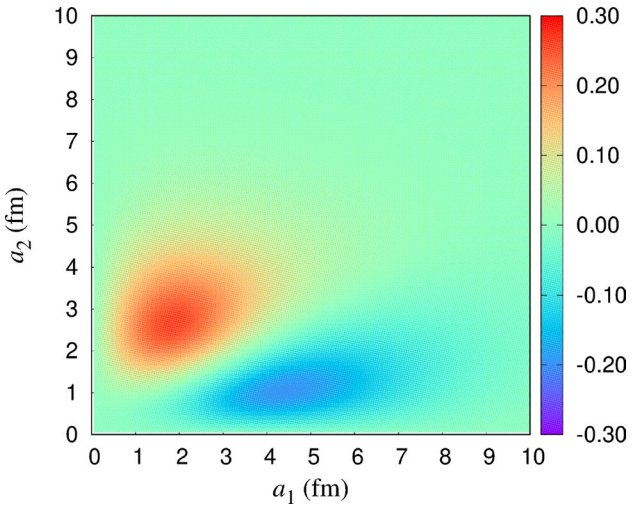

Fig. 14 (Color online) Calculated two-body overlap amplitude of the $[^8\mathrm{Be} \otimes [\mathrm{n} \otimes \mathrm{n}]_0]_0 \otimes [0 \otimes 0]_0$ channel in the ground state of ^{10}Be

with a "cigar" configuration, where the two valence neutrons are separated by a larger distance, whereas their COM is close to the α core. The area between the two peaks is narrow, with the overlap amplitude close to 0. This area corresponds to the three-body forbidden states, similar to the zero-value nodes that appear in RWA curves.

To observe the behavior of valence neutrons in the presence of a more complex core, we present the overlap amplitude of $^8\mathrm{Be} + \mathrm{n} + \mathrm{n}$ configuration in ^{10}Be in Fig. 14. The same configuration was previously analyzed with a smaller basis space [57]. We constructed a basis space with more spatial configurations by comprehensively considering the correlations between the clusters. As an analogous structure of $\alpha + \mathrm{n} + \mathrm{n}$ in ^{6}He, the $^8\mathrm{Be} + \mathrm{n} + \mathrm{n}$ configuration also exhibits two distinct areas associated with di-neutron and cigar correlations, with the amplitude peaks at ($r_1 = 1.8$ fm, $r_2 = 2.7$ fm) and ($r_1 = 4.4$ fm, $r_2 = 1.0$ fm), respectively. Compared to the $\alpha + \mathrm{n} + \mathrm{n}$ configuration, the amplitudes of $^8\mathrm{Be} + \mathrm{n} + \mathrm{n}$ are characterized by a more compact distribution, which is consistent with the smaller radius of ^{10}Be as compared with that of ^{6}He. Notably, our results agree well with the previous analysis of $^8\mathrm{Be} + \mathrm{n} + \mathrm{n}$ structure [57].

4.4 Reaction cross-section evaluation

The development of microscopic structure studies has led to the frequent adoption of microscopic structural information, including the RWA, as an important input in recent reaction calculations. The α knockout reaction, which is closely related to α clustering in nuclei, has been extensively studied to probe clustering structures or extract experimental SF values [95–97]. Recently, Yoshida et al. [30] analyzed the $^{20}\mathrm{Ne}(\mathrm{p}, \mathrm{p}\alpha)^{16}\mathrm{O}$ reaction, where the ^{16}O-α cluster wave function was obtained from a microscopically calculated RWA. The reaction and structural analyses demonstrated impressive consistency, as the experimental data were well reproduced without including any additional correction or scaling during the cross-section calculation.

Transfer reactions are also commonly used to extract structural information of nuclei [98]. By combining the CDCC and the improved DWBA via microscopic input of RWA, Chien and Descouvemont [51] studied the $^{16}\mathrm{C}(\mathrm{d}, \mathrm{p})^{17}\mathrm{C}$ transfer reaction and calculated the cross section, as shown in Fig. 15, and the microscopically calculated RWA. In this method, the wave functions of ^{16}C and ^{17}C are obtained using RGM. The $^{16}\mathrm{C} + \mathrm{d}$ and $^{17}\mathrm{C} + \mathrm{p}$ scattering wave functions are calculated using optical potential. For the entrance channel $^{16}\mathrm{C} + \mathrm{d}$, the breakup effects of the deuteron are simulated by the CDCC method. The cross sections are then obtained by evaluating the transfer scattering matrix. The calculated transfer cross sections show good agreement with the experimental data. Notably, no adjustable parameters were used during the calculation, and the results were insensitive to the choice of optical potential.

5 Summary and outlook

In this review, we presented the forms of various microscopic cluster model wave functions while considering some typical cluster models, including RGM, GCM, and OCM. We demonstrated the significance of the reduced-width amplitude, also known as the cluster form factor or overlap function, from the perspective of structure and reaction

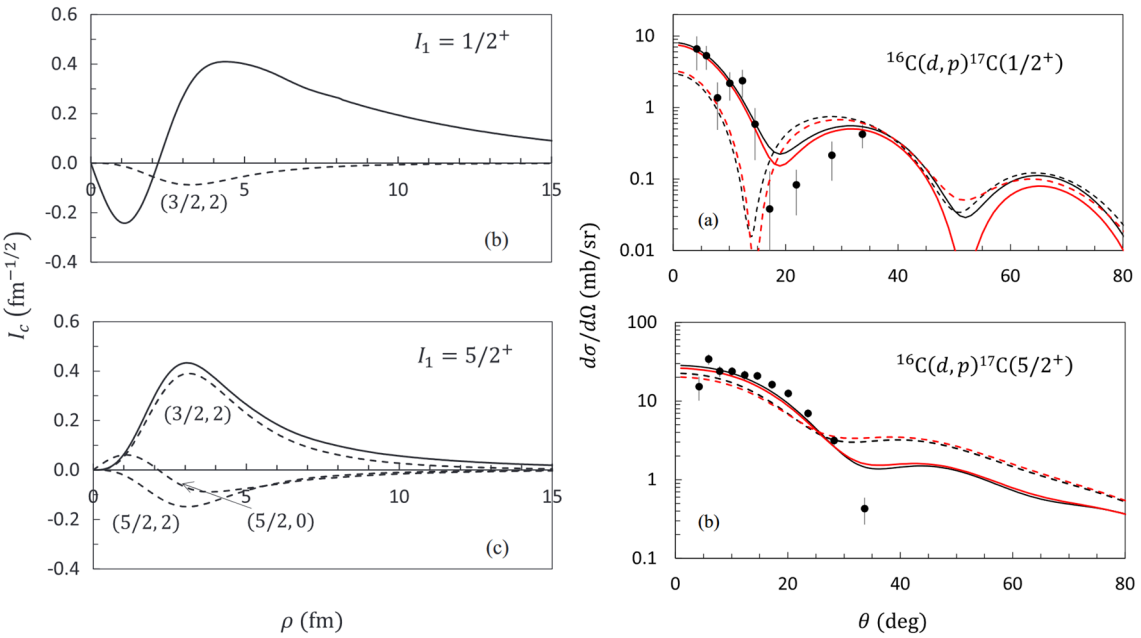

Fig. 15 RWAs of the ^{16}C + n channels in the $1/2^+$ and $5/2^+$ states of ^{17}C, and the ^{16}C$(d,p)^{17}$C transfer cross sections calculated using the RWA as input. The figure is taken from Ref. [51]

analyses. Based on the cluster model wave functions, we presented the definition and calculation methods of the RWA. The Laplace expansion is an effective approach to calculate the RWA, as compared to the traditional method, when the GCM or THSR wave function is constructed from the Brink cluster wave functions. Furthermore, the tail part of the RWA can be approximated by calculating the overlap between the nuclear and single-Brink wave functions. Following the brief theoretical framework that we revised, we presented some application examples to demonstrate the role played by RWA in the structure and reaction analyses of light nuclei. In addition, we extended the overlap amplitude calculation from the two-body to the three-body structure analysis for ^{6}He (α + n + n) and ^{10}Be (^{8}Be + n + n). Studies on three-body correlations in nuclear structures are currently in progress via the calculation of the two-body overlap amplitude.

References

1. M. Freer, H. Horiuchi, Y. Kanada-En'yo et al., Microscopic clustering in light nuclei. Rev. Mod. Phys. **90**, 035004 (2018). https://doi.org/10.1103/RevModPhys.90.035004
2. B. Zhou, Y. Funaki, H. Horiuchi et al., Nonlocalized clustering and evolution of cluster structure in nuclei. Front. Phys. **15**, 14401 (2019). https://doi.org/10.1007/s11467-019-0917-0
3. Y. Funaki, H. Horiuchi, A. Tohsaki, Cluster models from RGM to alpha condensation and beyond. Prog. Part. Nucl. Phys. **82**, 78–132 (2015). https://doi.org/10.1016/j.ppnp.2015.01.001
4. P. Descouvemont, M. Dufour, *Clusters in nuclei microscopic cluster models*, vol. 2 (Springer-Berlin, Heidelberg, 2012), pp.1–66
5. R.X. Cao, S. Zhang, Y.G. Ma, Effects of the α-cluster structure and the intrinsic momentum component of nuclei on the longitudinal asymmetry in relativistic heavy-ion collisions. Phys. Rev. C **108**, 064906 (2023). https://doi.org/10.1103/PhysRevC.108.064906
6. Z.W. Xu, S. Zhang, Y.G. Ma et al., Influence of α-clustering nuclear structure on the rotating collision system. Nucl. Sci. Tech. **29**, 186 (2018). https://doi.org/10.1007/s41365-018-0523-9
7. C.Z. Shi, Y.G. Ma, α-clustering effect on flows of direct photons in heavy-ion collisions. Nucl. Sci. Tech. **32**, 66 (2021). https://doi.org/10.1007/s41365-021-00897-9
8. K.J. Sun, R. Wang, C.M. Ko et al., Unveiling the dynamics of little-bang nucleosynthesis. Nat. Commun. **15**, 1074 (2024). https://doi.org/10.1038/s41467-024-45474-x
9. H. Pais, F. Gulminelli, C. Providência et al., Light and heavy clusters in warm stellar matter. Nucl. Sci. Tech. **29**, 181 (2018). https://doi.org/10.1007/s41365-018-0518-6
10. J. Tanaka, Z. Yang, S. Typel et al., Formation of α clusters in dilute neutron-rich matter. Science **371**, 260–264 (2021). https://doi.org/10.1126/science.abe4688
11. G. Röpke, Quasiparticle light elements and quantum condensates in nuclear matter. J. Phys: Conf. Ser. **321**, 012023 (2011). https://doi.org/10.1088/1742-6596/321/1/012023
12. J.A. Wheeler, On the mathematical description of light nuclei by the method of resonating group structure. Phys. Rev. **52**, 1107–1122 (1937). https://doi.org/10.1103/PhysRev.52.1107
13. H. Horiuchi, Chapter III. Kernels of GCM, RGM and OCM and their calculation methods. Prog. Theor. Phys. Supp. **62**, 90–190 (1977). https://doi.org/10.1143/PTPS.62.90
14. D.L. Hill, J.A. Wheeler, Nuclear constitution and the interpretation of fission phenomena. Phys. Rev. **89**, 1102–1145 (1953). https://doi.org/10.1103/PhysRev.89.1102

15. J.J. Griffin, J.A. Wheeler, Collective motions in nuclei by the method of generator coordinates. Phys. Rev. **108**, 311–327 (1957). https://doi.org/10.1103/PhysRev.108.311
16. S. Saito, Effect of Pauli principle in scattering of two clusters. Prog. Theor. Phys. **40**, 893–894 (1968). https://doi.org/10.1143/PTP.40.893
17. S. Saito, Interaction between clusters and Pauli principle. Prog. Theor. Phys. **41**, 705–722 (1969). https://doi.org/10.1143/PTP.41.705
18. S. Saito, Chapter II. Theory of resonating group method and generator coordinate method, and orthogonality condition model. Prog. Theor. Phys. Supp. **62**, 11–89 (1977). https://doi.org/10.1143/PTPS.62.11
19. A. Tohsaki, H. Horiuchi, P. Schuck et al., Alpha cluster condensation in ^{12}C and ^{16}O. Phys. Rev. Lett. **87**, 192501 (2001). https://doi.org/10.1103/PhysRevLett.87.192501
20. F. Hoyle, On nuclear reactions occuring in very hot stars. I. The synthesis of elements from carbon to nickel. Astrophys J Suppl Ser. **1**, 121 (1954). https://doi.org/10.1086/190005
21. B. Zhou, Y. Funaki, H. Horiuchi et al., Nonlocalized clustering: a new concept in nuclear cluster structure physics. Phys. Rev. Lett. **110**, 262501 (2013). https://doi.org/10.1103/PhysRevLett.110.262501
22. B. Zhou, Y. Funaki, H. Horiuchi et al., Nonlocalized cluster dynamics and nuclear molecular structure. Phys. Rev. C **89**, 034319 (2014). https://doi.org/10.1103/PhysRevC.89.034319
23. M. Lyu, Z. Ren, B. Zhou et al., Investigation of ^{9}Be from a nonlocalized clustering concept. Phys. Rev. C **91**, 014313 (2015). https://doi.org/10.1103/PhysRevC.91.014313
24. Y. Kanada-En'yo, T. Suhara, Y. Taniguchi, Approximation of reduced width amplitude and application to cluster decay width. Prog. Theor. Exp. Phys. (2014). https://doi.org/10.1093/ptep/ptu095
25. K. Wildermuth, Y.C. Tang, *A unified theory of the nucleus* (Vieweg+Teubner Verlag, Berlin, 1977)
26. P. Navrátil, Cluster form factor calculation in the ab initio no-core shell model. Phys. Rev. C **70**, 054324 (2004). https://doi.org/10.1103/PhysRevC.70.054324
27. N.K. Timofeyuk, Overlap functions for reaction theories: challenges and open problems. J. Phys. G **41**, 094008 (2014). https://doi.org/10.1088/0954-3899/41/9/094008
28. P. Descouvemont, A semi-microscopic approach to transfer reactions. Eur. Phys. J. A **58**, 193 (2022). https://doi.org/10.1140/epja/s10050-022-00840-5
29. S. Watanabe, K. Ogata, T. Matsumoto, Practical method for decomposing discretized breakup cross sections into components of each channel. Phys. Rev. C **103**, L031601 (2021). https://doi.org/10.1103/PhysRevC.103.L031601
30. K. Yoshida, Y. Chiba, M. Kimura et al., Quantitative description of the ^{20}Ne$(p,p\alpha)^{16}$O reaction as a means of probing the surface α amplitude. Phys. Rev. C **100**, 044601 (2019). https://doi.org/10.1103/PhysRevC.100.044601
31. M. Lyu, K. Yoshida, Y. Kanada-En'yo et al., Manifestation of α clustering in ^{10}Be via α-knockout reaction. Phys. Rev. C **97**, 044612 (2018). https://doi.org/10.1103/PhysRevC.97.044612
32. T. Fukui, Y. Taniguchi, T. Suhara et al., Probing surface distributions of α clusters in ^{20}Ne via α-transfer reaction. Phys. Rev. C **93**, 034606 (2016). https://doi.org/10.1103/PhysRevC.93.034606
33. G.R. Satchler, *Direct nuclear reactions* (Oxford University Press, Oxford, 1983)
34. N.K. Glendenning, *Distorted-wave born approximation in direct nuclear reactions* (Academic Press, Cambridge, 1983), pp.45–60
35. K. Ikeda, N. Takigawa, H. Horiuchi, The systematic structure-change into the molecule-like structures in the self-conjugate 4*n* nuclei. Prog. Theor. Phys. Supp. **E68**, 464–475 (1968). https://doi.org/10.1143/PTPS.E68.464
36. A.B. Volkov, Equilibrium deformation calculations of the ground state energies of 1p shell nuclei. Nucl. Phys. **74**, 33–58 (1965). https://doi.org/10.1016/0029-5582(65)90244-0
37. D.R. Thompson, M. Lemere, Y.C. Tang, Systematic investigation of scattering problems with the resonating-group method. Nucl. Phys. A **286**, 53–66 (1977). https://doi.org/10.1016/0375-9474(77)90007-0
38. H. Horiuchi, Generator coordinate treatment of composite particle reaction and molecule-like structures. Prog. Theor. Phys. **43**, 375–389 (1970). https://doi.org/10.1143/PTP.43.375
39. D. Brink, In: *Proceedings of the international school of physics "Enrico Fermi", Course 36, Varenna, 1965*, The alpha-particle model of light nuclei. Academic Press, (1966)
40. A. Ono, H. Horiuchi, T. Maruyama et al., Fragment formation studied with antisymmetrized version of molecular dynamics with two-nucleon collisions. Phys. Rev. Lett. **68**, 2898–2900 (1992). https://doi.org/10.1103/PhysRevLett.68.2898
41. A. Ono, H. Horiuchi, T. Maruyama et al., Antisymmetrized version of molecular dynamics with two-nucleon collisions and its application to heavy ion reactions. Prog. Theor. Phys. **87**, 1185–1206 (1992). https://doi.org/10.1143/ptp/87.5.1185
42. Y. Kanada-En'yo, H. Horiuchi, A. Ono, Structure of Li and Be isotopes studied with antisymmetrized molecular dynamics. Phys. Rev. C **52**, 628–646 (1995). https://doi.org/10.1103/PhysRevC.52.628
43. H. Feldmeier, Fermionic molecular dynamics. Nucl. Phys. A **515**, 147–172 (1990). https://doi.org/10.1016/0375-9474(90)90328-J
44. H. Feldmeier, K. Bieler, J. Schnack, Fermionic molecular dynamics for ground states and collisions of nuclei. Nucl. Phys. A **586**, 493–532 (1995). https://doi.org/10.1016/0375-9474(94)00792-L
45. H. Feldmeier, J. Schnack, Molecular dynamics for fermions. Rev. Mod. Phys. **72**, 655–688 (2000). https://doi.org/10.1103/RevModPhys.72.655
46. Y. Funaki, A. Tohsaki, H. Horiuchi et al., Analysis of previous microscopic calculations for the second 0^+ state in ^{12}C in terms of 3α particle bose-condensed state. Phys. Rev. C **67**, 051306 (2003). https://doi.org/10.1103/PhysRevC.67.051306
47. B. Zhou, Y. Funaki, A. Tohsaki et al., The container picture with two-alpha correlation for the ground state of ^{12}C. Prog. Theor. Exp. Phys. **2014**, 101D01 (2014). https://doi.org/10.1093/ptep/ptu127
48. B. Zhou, Y. Funaki, Container picture for 3^- and 4^- states of ^{12}C. Few-Body Syst. **63**, 26 (2022). https://doi.org/10.1007/s00601-021-01720-2
49. B. Zhou, New trial wave function for the nuclear cluster structure of nuclei. Prog. Theor. Exp. Phys. **2018**, 041D01 (2018). https://doi.org/10.1093/ptep/pty034
50. P. Descouvemont, D. Baye, The *R*-matrix theory. Rep. Prog. Phys. **73**, 036301 (2010). https://doi.org/10.1088/0034-4885/73/3/036301
51. L.H. Chien, P. Descouvemont, Analysis of the ^{16}C$(d,p)^{17}$C reaction from microscopic ^{17}C wave functions. Phys. Rev. C **108**, 044605 (2023). https://doi.org/10.1103/PhysRevC.108.044605
52. K. Yoshida, K. Ogata, Y. Kanada-En'yo, Investigation of α clustering with knockout reactions. Phys. Rev. C **98**, 024614 (2018). https://doi.org/10.1103/PhysRevC.98.024614
53. Y. Chiba, M. Kimura, Laplace expansion method for the calculation of the reduced-width amplitudes. Prog. Theor. Exp. Phys. **2017**, 053D01 (2017). https://doi.org/10.1093/ptep/ptx063
54. Y. Kanada-En'yo, Description of an α-cluster tail in ^{8}Be and ^{20}Ne: delocalization of the α cluster by quantum penetration. Prog. Theor. Exp. Phys. **2014**, 103D03 (2014). https://doi.org/10.1093/ptep/ptu121

55. P. Descouvemont, Spectroscopic amplitudes in microscopic three-cluster systems. Phys. Rev. C **107**, 014312 (2023). https://doi.org/10.1103/PhysRevC.107.014312
56. M. Kimura, Structure and decay of the pygmy dipole resonance in ^{26}Ne. Phys. Rev. C **95**, 034331 (2017). https://doi.org/10.1103/PhysRevC.95.034331
57. F. Kobayashi, Y. Kanada-En'yo, Analysis of the effect of core structure upon dineutron correlation using antisymmetrized molecular dynamics. Phys. Rev. C **93**, 024310 (2016). https://doi.org/10.1103/PhysRevC.93.024310
58. S. Baroni, P. Navrátil, S. Quaglioni, Ab initio description of the exotic unbound ^{7}He nucleus. Phys. Rev. Lett. **110**, 022505 (2013). https://doi.org/10.1103/PhysRevLett.110.022505
59. S. Baroni, P. Navrátil, S. Quaglioni, Unified ab initio approach to bound and unbound states: no-core shell model with continuum and its application to ^{7}He. Phys. Rev. C **87**, 034326 (2013). https://doi.org/10.1103/PhysRevC.87.034326
60. M. Vorabbi, P. Navrátil, S. Quaglioni et al., ^{7}Be and ^{7}Li nuclei within the no-core shell model with continuum. Phys. Rev. C **100**, 024304 (2019). https://doi.org/10.1103/PhysRevC.100.024304
61. C.W. Cook, W.A. Fowler, C.C. Lauritsen et al., ^{12}B,^{12} C, and the red giants. Phys. Rev. **107**, 508–515 (1957). https://doi.org/10.1103/PhysRev.107.508
62. H. Morinaga, Interpretation of some of the excited states of 4*n* self-conjugate nuclei. Phys. Rev. **101**, 254–258 (1956). https://doi.org/10.1103/PhysRev.101.254
63. H. Morinaga, On the spin of a broad state around 10 MeV in ^{12}C. Phys. Lett. **21**, 78–79 (1966). https://doi.org/10.1016/0031-9163(66)91349-7
64. Y. Suzuki, H. Horiuchi, K. Ikeda, Study of α chain states through their decay widths. Prog. Theor. Phys. **47**, 1517–1536 (1972). https://doi.org/10.1143/PTP.47.1517
65. E. Uegaki, Y. Abe, S. Okabe et al., Structure of the excited states in ^{12}C. II. Prog. Theor. Phys. **62**, 1621–1640 (1979). https://doi.org/10.1143/PTP.62.1621
66. M. Kamimura, Transition densities between the 0_1^+, 2_1^+, 4_1^+, 0_2^+, 2_2^+, 1_1^- and 3_1^- states in ^{12}C derived from the three-alpha resonating-group wave functions. Nucl. Phys. A **351**, 456–480 (1981). https://doi.org/10.1016/0375-9474(81)90182-2
67. P. Descouvemont, D. Baye, Microscopic theory of the ^{8}Be$(\alpha,\gamma)^{12}$C reaction in a three-cluster model. Phys. Rev. C **36**, 54–59 (1987). https://doi.org/10.1103/PhysRevC.36.54
68. B. Zhou, A. Tohsaki, H. Horiuchi et al., Breathing-like excited state of the Hoyle state in ^{12}C. Phys. Rev. C **94**, 044319 (2016). https://doi.org/10.1103/PhysRevC.94.044319
69. Y. Funaki, T. Yamada, A. Tohsaki et al., Microscopic study of 4α -particle condensation with inclusion of resonances. Phys. Rev. C **82**, 024312 (2010). https://doi.org/10.1103/PhysRevC.82.024312
70. Y. Funaki, T. Yamada, H. Horiuchi et al., α-particle condensation in ^{16}O studied with a full four-body orthogonality condition model calculation. Phys. Rev. Lett. **101**, 082502 (2008). https://doi.org/10.1103/PhysRevLett.101.082502
71. B. Zhou, Y. Funaki, H. Horiuchi et al., The 5α condensate state in ^{20}Ne. Nat. Commun. **14**, 8206 (2023). https://doi.org/10.1038/s41467-023-43816-9
72. M. Kimura, Deformed-basis antisymmetrized molecular dynamics and its application to ^{20}Ne. Phys. Rev. C **69**, 044319 (2004). https://doi.org/10.1103/PhysRevC.69.044319
73. Y. Liu, Y.L. Ye, Nuclear clustering in light neutron-rich nuclei. Nucl. Sci. Tech. **29**, 184 (2018). https://doi.org/10.1007/s41365-018-0522-x
74. A.A. Korsheninnikov, E.Y. Nikolskii, T. Kobayashi et al., Spectroscopy of ^{12}Be and ^{13}Be using a ^{12}Be radioactive beam. Phys. Lett. B **343**, 53–58 (1995). https://doi.org/10.1016/0370-2693(94)01435-F
75. W. von Oertzen, Two-center molecular states in ^{9}B,^{9} Be, ^{10}Be, and ^{10}B. Z. Phys. A **354**, 37–43 (1996). https://doi.org/10.1007/s002180050010
76. W. von Oertzen, Dimers based on the $\alpha+\alpha$ potential and chain states of carbon isotopes. Z. Phys. A **357**, 355–365 (1997). https://doi.org/10.1007/s002180050255
77. K. Arai, Structure of the excited states of ^{10}Be in a microscopic cluster model. Phys. Rev. C **69**, 014309 (2004). https://doi.org/10.1103/PhysRevC.69.014309
78. K. Arai, P. Descouvemont, D. Baye et al., Resonance structure of ^{9}Be and ^{9}B in a microscopic cluster model. Phys. Rev. C **68**, 014310 (2003). https://doi.org/10.1103/PhysRevC.68.014310
79. S. Okabe, Y. Abe, The structure of ^{9}Be by a molecular model. II. Prog. Theor. Phys. **61**, 1049–1064 (1979). https://doi.org/10.1143/PTP.61.1049
80. Q. Zhao, Y. Suzuki, J. He et al., α clustering and neutron-skin thickness of carbon isotopes. Eur. Phys. J. A **57**, 157 (2021). https://doi.org/10.1140/epja/s10050-021-00465-0
81. Y. Kanada-En'yo, H. Horiuchi, Cluster structures of the ground and excited states of ^{12}Be studied with antisymmetrized molecular dynamics. Phys. Rev. C **68**, 014319 (2003). https://doi.org/10.1103/PhysRevC.68.014319
82. H. Motoki, Y. Suzuki, T. Kawai et al., Cluster formation in neutron-rich Be and B isotopes. Prog. Theor. Exp. Phys. **2022**, 113D01 (2022). https://doi.org/10.1093/ptep/ptac145
83. Y. Chiba, M. Kimura, Hoyle-analog state in ^{13}C studied with antisymmetrized molecular dynamics. Phys. Rev. C **101**, 024317 (2020). https://doi.org/10.1103/PhysRevC.101.024317
84. Y. Kanada-En'yo, Negative parity states of ^{11}B and ^{11}C and the similarity with ^{12}C. Phys. Rev. C **75**, 024302 (2007). https://doi.org/10.1103/PhysRevC.75.024302
85. T. Yamada, Y. Funaki, $\alpha+\alpha+t$ cluster structures and ^{12}C(0_2^+) -analog states in ^{11}B. Phys. Rev. C **82**, 064315 (2010). https://doi.org/10.1103/PhysRevC.82.064315
86. B. Zhou, M. Kimura, $2\alpha+t$ cluster structure in ^{11}B. Phys. Rev. C **98**, 054323 (2018). https://doi.org/10.1103/PhysRevC.98.054323
87. T. Yamada, Y. Funaki, α-cluster structures and monopole excitations in ^{13}C. Phys. Rev. C **92**, 034326 (2015). https://doi.org/10.1103/PhysRevC.92.034326
88. M.V. Mihailović, M. Poljšak, The interplay of cluster structures in light nuclei: the model and the application to ^{7}Li. Nucl. Phys. A **311**, 377–394 (1978). https://doi.org/10.1016/0375-9474(78)90520-1
89. K. Toshitaka, M. Takehiro, A. Akito, Effect of breathing excitations of the triton nucleus on the αt cluster structure of ^{7}Li. Nucl. Phys. A **414**, 185–205 (1984). https://doi.org/10.1016/0375-9474(84)90639-0
90. T. Kaneko, M. Shirata, H. Kanada et al., Microscopic theory of the ^{3}H $+\alpha$ system with the multichannel resonating-group method. Phys. Rev. C **34**, 771–779 (1986). https://doi.org/10.1103/PhysRevC.34.771
91. U.G. Meißner, B.C. Metsch, Probing nuclear observables via primordial nucleosynthesis. Eur. Phys. J. A **58**, 212 (2022). https://doi.org/10.1140/epja/s10050-022-00869-6
92. B.S. Huang, Y.G. Ma, Two-proton momentum correlation from photodisintegration of α-clustering light nuclei in the quasideuteron region. Phys. Rev. C **101**, 034615 (2020). https://doi.org/10.1103/PhysRevC.101.034615
93. L. Ma, Y.G. Ma, S. Zhang, Anisotropy fluctuation and correlation in central α-clustered ^{12}C+^{197}Au collisions. Phys. Rev. C **102**, 014910 (2020). https://doi.org/10.1103/PhysRevC.102.014910
94. K. Hagino, A. Vitturi, F. Pérez-Bernal et al., Two-neutron halo nuclei in one dimension: dineutron correlation and breakup

reaction. J. Phys. G **38**, 015105 (2010). https://doi.org/10.1088/0954-3899/38/1/015105
95. P.J. Li, D. Beaumel, J. Lee et al., Validation of the ^{10}Be ground-state molecular structure using ^{10}Be$(p,p\alpha)^{6}$He triple differential reaction cross-section measurements. Phys. Rev. Lett. **131**, 212501 (2023). https://doi.org/10.1103/PhysRevLett.131.212501
96. J. Mabiala, A.A. Cowley, S.V. Förtsch et al., Analyzing power and cross section distributions of the ^{12}C$(p,p\alpha)^{8}$Be cluster knock-out reaction at an incident energy of 100 MeV. Phys. Rev. C **79**, 054612 (2009). https://doi.org/10.1103/PhysRevC.79.054612
97. T. Yoshimura, A. Okihana, R. Warner et al., Alpha spectroscopic factors for ^{6}Li,^{7} Li, ^{9}Be and ^{12}C from the $(p,p\alpha)$ reaction at 296 MeV. Nucl. Phys. A **641**, 3–20 (1998). https://doi.org/10.1016/S0375-9474(98)00432-1
98. W. Liu, J.L. Lou, Y.L. Ye et al., Experimental study of intruder components in light neutron-rich nuclei via single-nucleon transfer reaction. Nucl. Sci. Tech. **31**, 20 (2020). https://doi.org/10.1007/s41365-020-0731-y